

Predicting Ti-Al Binary Phase Diagram with an Artificial Neural Network Potential

Micah Nichols, Christopher D. Barrett, and Doyl E. Dickel*

*Michael W. Hall School of Mechanical Engineering and
Center for Advanced Vehicular Systems, Mississippi State University,
Mississippi State, Mississippi 39762, USA*

Mashroor S. Nitol and Saryu J. Fensin

Los Alamos National Laboratory, Los Alamos, NM, 87545, USA

Abstract

The microstructure of the Ti-Al binary system is an area of great interest as it affects material properties and plasticity. Phase transformations induce microstructural changes; therefore, accurately modeling the phase transformations of the Ti-Al system is necessary to describe plasticity. Interatomic potentials can be a powerful tool to model how materials behave; however, existing potentials lack accuracy in certain aspects. While classical potentials like the Embedded Atom Method (EAM) and Modified Embedded Atom Method (MEAM) perform adequately for modeling dilute Al solute within Ti's α phase, they struggle with accurately predicting plasticity. In particular, they struggle with stacking fault energies in intermetallics and to some extent elastic properties. This hinders their effectiveness in investigating the plastic behavior of formed intermetallics in Ti-Al alloys. Classical potentials also fail to predict the α to β phase boundary. Existing machine learning (ML) potentials reproduce the properties of formed intermetallics with density functional theory (DFT) but do not examine the α to β or α to D0₁₉ phase boundaries. This work uses a rapid artificial neural network (RANN) framework to produce a neural network potential for the Ti-Al binary system. This potential is capable of reproducing the Ti-Al binary phase diagram up to 50% Al concentration. The present interatomic potential ensures stability and allows results near the accuracy of DFT. Using Monte Carlo simulations, RANN potential accurately predicts the α to β and α to D0₁₉ phase transitions. The current potential also exhibits accurate elastic constants and stacking fault energies for the L1₀ and D0₁₉ phases.

Keywords: Titanium, Aluminum, phase transition, molecular dynamics, machine learning, intermetallics

* doyl@me.msstate.edu

I. INTRODUCTION

Ti-Al alloys are indispensable due to their high melting points, exceptional specific strength and stiffness, and excellent resistance to oxidation and corrosion [1]. These properties make them suitable for load-carrying applications in aerospace, automotive, and energy industries [2, 3]. While Ni-based superalloys have traditionally dominated these fields, Ti-Al alloys exhibit comparable performances at temperatures ranging between 600 and 800 °C [4]. The ability of Ti-Al alloys, particularly the two-phase intermetallics like L1₀ γ -TiAl and D0₁₉ α_2 -Ti₃Al, to operate efficiently at elevated temperatures while maintaining resistance to oxidation and creep underscores their technological importance [5, 6]. The microstructure within Ti-Al alloys changes significantly with composition. At low Al concentrations, Ti has a low temperature α (HCP) phase, and a high temperature β (BCC) phase. At an Al concentration around 12%, the ordered hexagonal D0₁₉ (α_2) phase forms. These phases, in turn, affect material properties such as ductility, fracture toughness, and creep resistance. For instance, lamellar γ -TiAl, with a combination of γ and α_2 phases, exhibits superior high-temperature performance but suffers from poor room-temperature ductility due to its complex dislocation slip and twinning systems [7]. Studying phase evolution within Ti-Al alloys is crucial for understanding and enhancing their mechanical behavior under operational conditions. Phase transformations dictate the material's structural integrity and performance, particularly under thermal cycling, which is common in aerospace applications [8, 9]. Understanding these transformations helps in optimizing alloy compositions and heat treatment processes to achieve desired mechanical properties.

Molecular dynamics (MD) simulations play a pivotal role in the modeling of Ti-Al alloys by utilizing atomic-scale interactions to reproduce phenomena that can be challenging to observe experimentally. These simulations provide insights into the mechanisms of plastic deformation, phase transitions, and the impact of alloying elements on the material's properties. Furthermore, MD can predict the behavior of materials under various loading and environmental conditions, thus aiding in the design of more resilient materials. Both experimental and computational methodologies have been used in the extensive study of Ti-Al alloys to interpret the complex interplay of alloy composition, microstructure, and mechanical properties [10–12]. Historically, experimental approaches, such as in-situ transmission electron microscopy (TEM) experiments, have provided significant insights into basic

deformation mechanisms, interface strengthening behaviors, and crack nucleation and propagation in these alloys. These studies have elucidated the role of microstructural features like grain and interphase boundaries in governing plasticity and fracture behaviors [13, 14]. Computational research efforts have primarily focused on the use of density functional theory (DFT) [12, 15–17] and empirical or semi-empirical interatomic potentials such as the Embedded-Atom Method (EAM) [18–20] and the Modified Embedded-Atom Method (MEAM) [21–23] to describe the microstructural features in Ti-Al alloys. DFT calculations have shed light on the non-planar character of dislocation cores and their associated Peierls stresses, offering deep insights at the atomic scale. One major drawback in using these quantum mechanics-based methods is the computational demand required when simulating complex dislocations or large systems [24–26].

Empirical potentials, while useful in overcoming the size and time limitations of DFT, often fall short in accuracy. For instance, EAM and MEAM potentials have been tailored to capture the directional bonding essential for modeling Ti-Al alloys but have shown discrepancies in modeling the full spectrum of plasticity and fracture phenomena across different stable phases [27]. This has led to a partial understanding that lacks the ability to comprehensively predict material behavior under varied operational conditions, particularly at high temperatures.

To address these challenges, a paradigm shift has emerged in the field of materials science, wherein machine learning (ML) techniques are leveraged to develop interatomic potentials [28–35]. ML potentials represent a departure from conventional methods, minimizing reliance on physical or chemical intuition by interpolating mathematical functions using reference data obtained from DFT computations. This data-driven approach has revolutionized computational materials science, accelerating the discovery of new materials by accurately capturing the underlying physics of interatomic bonding. Some of the more popular ML potentials include the spectral neighbor analysis method (SNAP), Gaussian approximation potentials (GAP), spline-based neural network potentials (s-NNP), and moment tensor potentials (MTP) [29, 36–38]. For the Ti-Al system, the most prominent ML potential employs the MTP [39] formalism and exhibits superior accuracy when compared to previous ML potential [40]. Despite this accuracy, MTP does not adequately capture the transition between pure Ti and its intermetallics. While it demonstrates excellent accuracy within the intermetallic phases, it fails to accurately predict phase evolution and the effects of solutes

on the plasticity of pure Ti's α and β phases.

Building on the foundation laid by previous research, the current study introduces significant advancements in the molecular dynamics simulation of Ti-Al alloys through the development and implementation of the Rapid Artificial Neural Network (RANN) framework [41–45]. This novel approach leverages machine learning to interpolate complex potential energy surfaces from a vast dataset derived from high-fidelity DFT calculations. Unlike previous interatomic potentials, RANN is capable of modeling both the dilute and intermetallic phases of Ti-Al alloys with a level of precision comparable to DFT calculations. RANN is also effective in seamlessly transitioning between different alloy phases without a loss in accuracy. This is particularly important for Ti-Al alloys, where phase evolution plays a critical role in determining material properties. To the best of authors' knowledge, no existing interatomic potential comprehensively models both the dilute alloy and intermetallic phases of this crucial alloy at the atomistic scale. The current study bridges the gap between the modeling capabilities of dilute alloys and intermetallics of Ti-Al. Here, RANN is designed to be inherently flexible, enabling it to accurately predict phase behaviors, solute effects, and the thermomechanical properties of both dilute and intermetallic phases.

II. METHODOLOGY

A. First principle calculations

A DFT database was created using version 6.3.2 of the Vienna Ab initio Simulation Package (VASP) [46]. The simulations utilized the generalized gradient approximation (GGA) with the Perdew-Burke-Ernzerhof (PBE) [47] exchange-correlation functional. A densely packed Monkhorst-Pack k -mesh was implemented to ensure accuracy and maintained a minimum distance between neighboring k -points of $2\pi \times 0.01\text{\AA}^{-1}$ in reciprocal lattice units. The electronic wave functions were expanded using a kinetic energy cutoff of 520 eV, and a Gaussian smearing of 0.2 eV smoothed the integration over the Brillouin zone.

The database contains data with up to 15% equilibrium lattice distortion for BCC, FCC, HCP, $a15$, $\beta - Sn$, SC, and DC structures in both pure and alloyed forms of Ti and Al. It also contains up to 15% equilibrium lattice distortions for ordered intermetallic structures such as γ -TiAl and D0₁₉-Ti₃Al. For all the previously mentioned structures, additional

simulations displace the atoms by random vectors with a magnitude of up to 0.5 Å as well as random independent distortions of the simulation box lengths and angles up to $\pm 5\%$ to simulate finite temperature behavior between 100 K and 2200 K. Stacking faults, vacancies, free surface, and amorphous configurations for Ti, Al, and Ti-Al alloys were also included. A detailed table showing all data used for training can be found in the supplemental materials [48].

B. RANN

RANN uses a multilayer perceptron artificial neural network and begins with an input layer that captures a structural fingerprint, characterizing the local atomic environment for each atom based on the MEAM formalism [49–51]. Two types of structural fingerprints are employed – a pair interaction fingerprint and a three body fingerprint. The pair interaction is described by:

$$F_n = \sum_{j \neq i} \left(\frac{r_{ij}}{r_e} \right)^n e^{-\alpha_n \frac{r_{ij}}{r_e}} f_c \left(\frac{r_c - r_{ij}}{\Delta r} \right) S_{ij} \quad (2.1)$$

where r_e is the equilibrium nearest neighbor distance, r_c is a cutoff distance to determine the neighbors, j , of atom i , n is an integer, α_n is related to the bulk modulus as used in MEAM [51], and S_{ij} is an angular screening term. The three body term is described by:

$$G_{m,k} = \sum_{j,k} \cos^m \theta_{jik} e^{-\beta_k \frac{r_{ij} + r_{ik}}{r_e}} f_c \left(\frac{r_c - r_{ij}}{\Delta r} \right) \times f_c \left(\frac{r_c - r_{ik}}{\Delta r} \right) S_{ij} S_{ik} \quad (2.2)$$

where m is an integer, θ_{jik} describes the angle between the vectors from atom i to atom j and atom i to atom k , and β_k determines the length scale. Each type of fingerprint uses angular screening to reduce the neighbor list, therefore improving computational efficiency. Each layer is input into a nonlinear activation function. The result of the activation function combined with weights and biases determine the values for the next layer. 10% of the data from each sample set is reserved for validation purposes. The Levenberg-Marquardt (LM) algorithm [52, 53], noted for its efficiency over traditional gradient descent methods in machine learning interatomic potentials (MLIPs) [54], is utilized for training. To prevent overfitting and boost the model’s accuracy, a regularization term of $\lambda = 1 \times 10^{-4}$ is added

to the loss function described by:

$$L_{MSE} = \frac{1}{m} \sum (\hat{Y} - Y)^2 + \frac{\lambda}{2m} \sum \|W\|_F^2 \quad (2.3)$$

where \hat{Y} is the energy predicted by the network, Y is the energy from DFT, and m is the number of training points. The output layer will always consist of one node that represents the energy of a particular atom. More information on the RANN formalism can be found in the works of Dickel et al. [35] and Nitol et al. [43]. The LAMMPS implementation of RANN can be found at <https://github.com/ranndip/ML-RANN>.

C. Generalized stacking fault energies

When validating the generalized stacking fault energies (GSFE), we focus on the basal, pyramidal I, pyramidal II, and prismatic slip systems for the α and $D0_{19}$ phases, the (1 1 0) plane for the β phase, and the (1 1 1) plane for the $L1_0$ phase. For the α and β phases, the GSFE was computed for pure Ti first. Then, one Ti atom was swapped to an Al atom to observe the impact solute Al has on the GSFE. The structures used to obtain the GSFE curves were created using the atomman Python package [55, 56]. The simulation cells ranged from 20-80 atoms depending on structure and orientation. The fault plane was placed at approximately the middle of the cell. Different structures were created by moving the atoms above the fault plane in two independent directions until the original configuration was reached. The structures were then put into a LAMMPS simulation containing periodic boundary conditions in the x and y directions and a free surface normal to the glide plane (z direction). The atoms were allowed to relax in the z direction but could not move in the x or y directions.

D. Phase Diagram

The phase diagram simulations are split into two parts: the α to $D0_{19}$ transition and the α to β transition. The α to $D0_{19}$ transition employs the semi-grand-canonical Monte Carlo (MC) [57] method in LAMMPS. The technique used in this work was motivated from the work of Kim et al. [23] Pure α -Ti was equilibrated to the desired temperature and given a chemical potential value (μ). The semi-grand-canonical MC fix in LAMMPS employs the

Metropolis acceptance criterion [58] with the addition of a chemical potential difference term, $\Delta\mu$. This fix attempts to swap a Ti atom with an Al atom 10 times for every MD timestep and accepts the swap according to the Metropolis algorithm [58]. More information about the acceptance probability can be found in the work of Sadigh et al. [57]. The simulations consisted of 1024 atoms and were run at varying temperatures for 40 ps. The same was done with a D0₁₉ structure. By plotting the equilibrated atomic percentage of Al against $\Delta\mu$ for the initial α structure and the D0₁₉ structure, a hysteresis loop can be found. The final atomic percentage of Al before the α phase jumps to the D0₁₉ phase corresponds to the phase transition point for the α to D0₁₉ transition. The final atomic percentage of Al before the D0₁₉ phase spontaneously becomes the α phase corresponds to the phase transition point of the D0₁₉ to α transition.

The method to obtain the α to β phase boundary involved several simulations and was based on the work of Dickel et al. [41]. Simulations were run for Al concentrations from 0% to 20% Al in 2.5% increments. For structures containing Al, MC MD simulations were used to place solute Al in their preferred lattice sites. First, the enthalpy of the α , β , and liquid phases must be found as a function of temperature for varying concentrations of Al. These enthalpies are used in the calculation of the relative Gibbs free energy described later. Next, simulations inducing a solid-liquid interface must be run. The following steps describe simulations for the α -liquid interface; however, the same procedure was used for the β -liquid interface simulations. An α phase simulation cell composed of 27,648 atoms was heated to 1000 K over 5 ps. Half of the cell was then heated over 5 ps to induce an amorphous region. Next, a constant enthalpy calculation (nph) was applied. This allowed the cell to change size in the direction normal to the solid-liquid interface to equilibrate at zero pressure. The equilibrated temperature was considered the melting point. Once this was complete, the Gibbs-Helmholtz relation can be integrated to calculate the relative Gibbs free energy. The Gibbs-Helmholtz relation is defined by:

$$\left(\frac{\partial \left(\frac{G(T)}{T} \right)}{\partial T} \right)_p = -\frac{H(T)}{T^2} \quad (2.4)$$

where the Gibbs free energy and the enthalpy of the system at some temperature, T, is given by $G(T)$ and $H(T)$, respectively. After integration, the relative Gibbs free energy, ΔG , was found, and the transition temperature between the α and β phases was taken to

be the temperature at which $\Delta G = 0$.

III. RESULTS

A. Potential Creation

Fig. 1 illustrates the development of the RANN potential using a multilayer perceptron artificial neural network, adapted from the methods described by Dickel et al. [35]. The previously mentioned DFT database used to train the potential includes a total of 62,724 simulations and 2,830,192 unique atomic environments. Each fingerprint used in the creation of the RANN potential contains metaparameters that can be adjusted to improve accuracy. Once the desired accuracy is achieved, the new potential undergoes primary validation. Primary validation includes checking the lattice parameter, elastic constants, ground-state structure, etc. against the values given by DFT to ensure that the potential has properly trained over the DFT database. If any of the tests yield incorrect results, new DFT data can be generated to inform the network of any missing information. Once the potential passes primary validation, it is tested for its capability of predicting phase boundaries. If the potential fails to predict the proper phase boundaries, new DFT data can be generated to inform the network, and the cycle begins again. The Ti-Al RANN potential can be found at <https://github.com/ranndip/RANN-potentials/blob/main/TiAl.nn>.

The RANN potential incorporates a single hidden layer within its network architecture, consisting of 26 neurons for the Ti network and 22 neurons for the Al network. The architecture is explicitly defined as $58 \times 26 \times 1$ for Ti and $50 \times 22 \times 1$ for Al, where 58 and 50 features describe the structural fingerprints for Ti and Al respectively. The metaparameters used for both networks can be found below in **Table I**.

The network's performance is evaluated by aggregating the outputs for all atoms in a simulation and comparing these results with total energies derived from DFT calculations. The root mean square error (RMSE) is calculated and employed as the loss function, which is minimized to refine the weights and biases. Post-training, the RMSE for the training and validation datasets are recorded at 4.68 meV/atom and 4.98 meV/atom, respectively, for the Ti-Al dataset. The high validation accuracy highlights the model's reliability and indicates that the potential is likely able to reproduce structures contained in the dataset within a

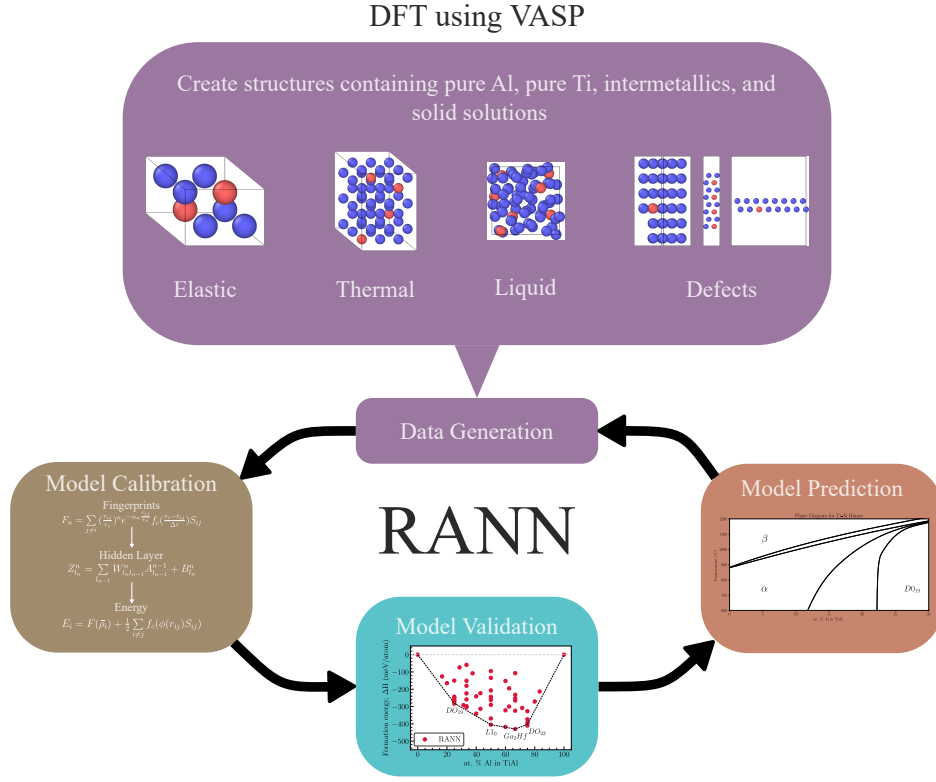


Figure 1. Summary of the RANN potential development workflow.

Table I. Metaparameters for Ti and Al.

Fingerprint metaparameters	Ti	Al
m	$\in \{0...6\}$	$\in \{0...5\}$
n	$\in \{-1...3\}$	$\in \{-1...3\}$
r_e (\AA)	2.924308	2.856975
α	4.72	4.685598
β_k	1,2,5,9	1,2,5,9
r_c (\AA)	8.0	8.0
Δr (\AA)	5.075692	5.143025
C_{min}	0.49	0.49
C_{max}	1.44	1.44

4.98 meV/atom margin of error.

B. Primary Validation

Fig. 2 shows an energy vs volume curve for α , β , ω , and FCC phases in pure Ti as well as FCC, BCC, and HCP phases in pure Al. RANN predicts the α and ω phases to be the low energy structures in pure Ti in agreement with DFT results. In pure Al, RANN follows DFT in predicting the FCC phase to be the lowest energy phase.

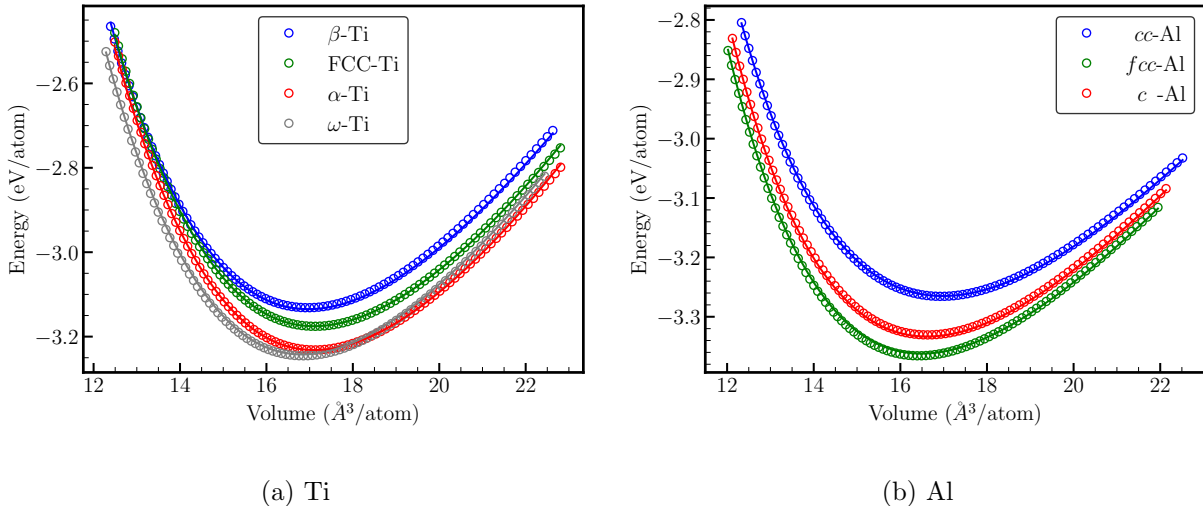
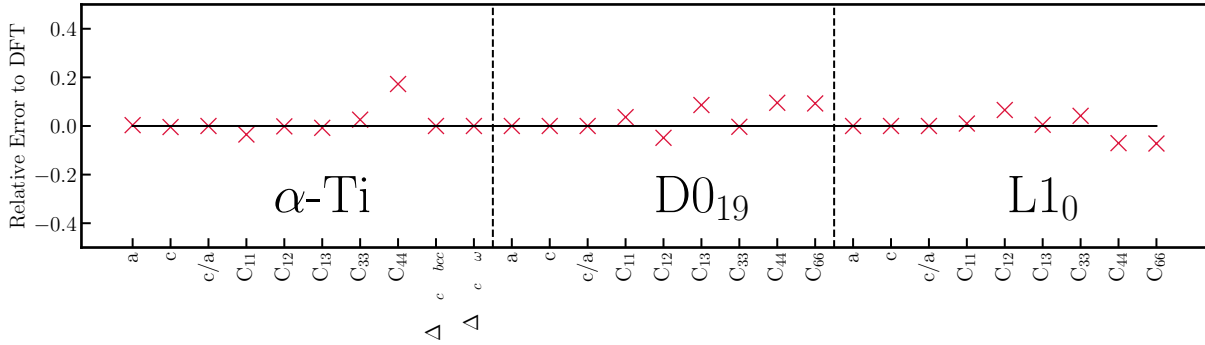


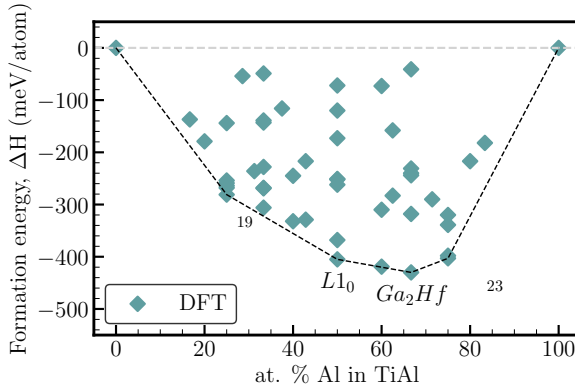
Figure 2. EV curves for (a) Ti and (b) Al. Circles represent DFT and lines represent RANN.

Fig. 3 shows the lattice parameters and elastic constants for pure α -Ti, D0₁₉, and L1₀ phases as well as the convex hull for RANN compared to DFT. RANN is in good agreement with DFT calculations. The C_{44} elastic constant for α -Ti deviates the furthest from DFT at 17%; however, the average deviation across these properties is 1.4%. Both RANN and DFT show that the D0₁₉, L1₀, Ga₂Hf, and D0₂₃ structures are the low energy structures with increasing Al concentration. In order for the potential to accurately model the Ti-Al system, it must show that Al is soluble in Ti. DFT gives the substitutional energy of Al in Ti for the stable α phase to be -829 *meV*. RANN shows the substitutional energy to be -849 *meV*; therefore, RANN correctly predicts Al to be soluble in Ti. More information on the material properties for various phases can be found in the supplemental information [48] (see also references [12, 15, 27, 42, 59–84] therein).

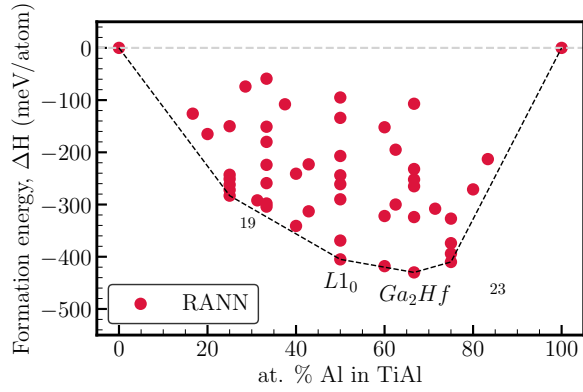
Predicting the forces acting on individual atoms can be an indicator on how well an atomic potential will succeed in accurately displaying results for dynamic simulations. Here, the x , y , and z components of the force acting on individual atoms for finite temperature per-



(a) Relative error for RANN compared to DFT



(b) Convex hull for DFT



(c) Convex hull for RANN

Figure 3. (a) RANN material properties for α -Ti, D0₁₉, and L1₀ compared to DFT. (b) Convex hull for DFT and (c) RANN.

turbations of α -Ti, β -Ti, and ω -Ti structures are computed using DFT as well as with the RANN potential. While possible to train potentials over forces and energies from DFT, the RANN potential created in this work only trains over atomic energies. Shown in Fig. 4, RANN shows a RMSE of 0.12 eV/Å, 0.11 eV/Å, and 0.17 eV/Å for α -Ti, β -Ti, and ω -Ti, respectively.

C. GSFE Validation

The presence of solute atoms along glide planes can significantly influence dislocation mechanisms. This is vital because dislocations are the main vectors of plastic deformation in metals. By understanding the interaction between solutes and dislocations, we can better

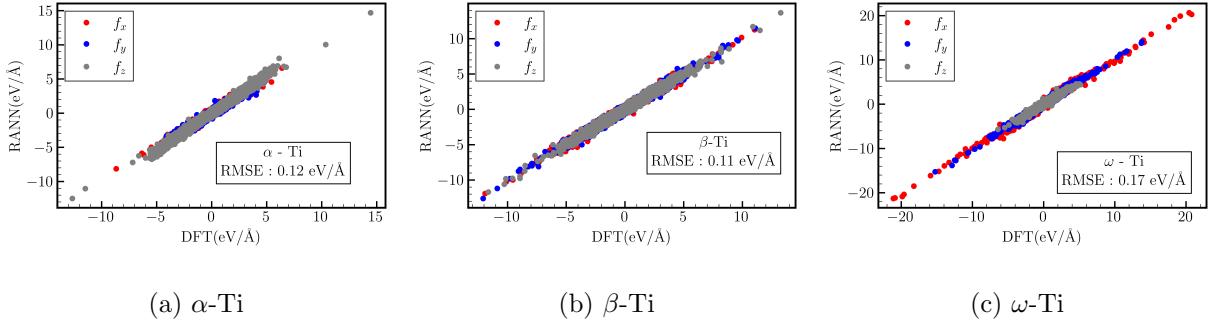


Figure 4. Force comparison for (a) α -Ti, (b) β -Ti, and (c) ω -Ti.

predict and manage the mechanical properties of alloys. Previous studies, such as those using generalized stacking fault energy (GSFE) calculations, have demonstrated how these interactions can enhance properties like strength, ductility, and toughness [85]. For instance, specific solute atoms may obstruct dislocation movement, contributing to solid solution strengthening. In Ti-Al alloys, Al solutes disrupt the emission of prismatic dislocations and alter the energy of basal/prismatic faults. This effect helps to stabilize the immobile, non-planar core of screw $1/3\langle 11\bar{2}0 \rangle$ dislocations, significantly enhancing the strength of α -Ti [86]. Understanding GSFE and the influence of solute positioning allows for the tailoring of alloy compositions to achieve desired mechanical traits, crucial for designing alloys for specific applications requiring high strength or improved ductility.

RANN is in good agreement with DFT for both the pure Ti case as well as when solute Al is adjacent to the glide plane. RANN shows softening in the basal plane when Al is near the glide plane as expected. Both RANN and DFT results also show a stiffening in the prismatic plane after an Al atom is placed adjacent to the glide plane. Fig. 5 shows the GSFE for the mentioned planes.

The GSFE was also calculated for several planes in the formed intermetallic phases. The basal, pyramidal I, pyramidal II, prismatic narrow, prismatic wide I, and prismatic wide II planes were examined for the $D0_{19}$ phase, and the (111) plane was examined for the $L1_0$ phase. MTP is very accurate in predicting the GSFE for intermetallics [39]. Shown in Fig. 6, Rann is found to be in agreement with the the GSFE predicted by MTP for intermetallic structures. A comparison of the GSFE with one solute Al atom between DFT, MTP [39], and MEAM [23] can be found in the supplemental information [48].

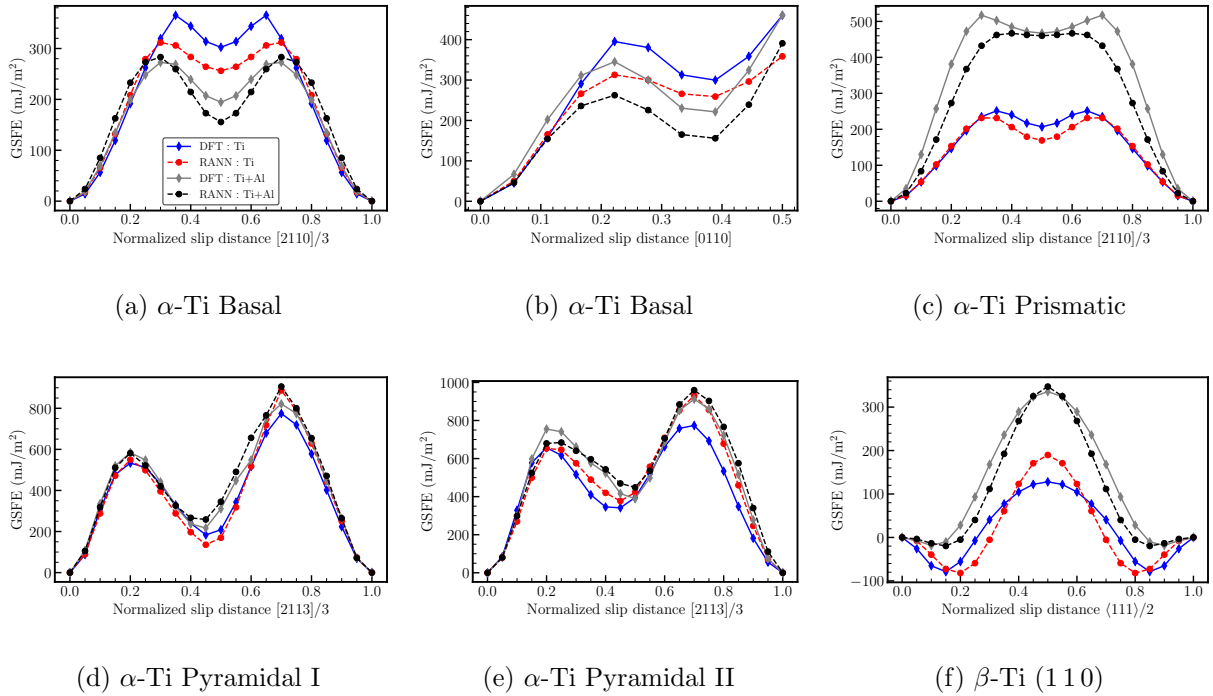
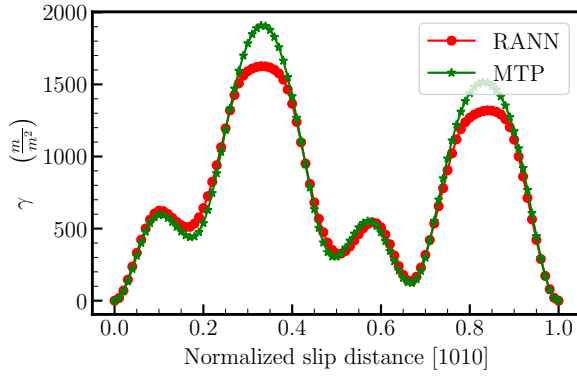


Figure 5. GSFE of Ti-Al alloy, where solute Al’s position is in first nearest positions relative to the glide plane for the (a-b) Basal, (c) Prismatic, (d) Pyramidal I, (e) Pyramidal II, and (f) (110) planes.

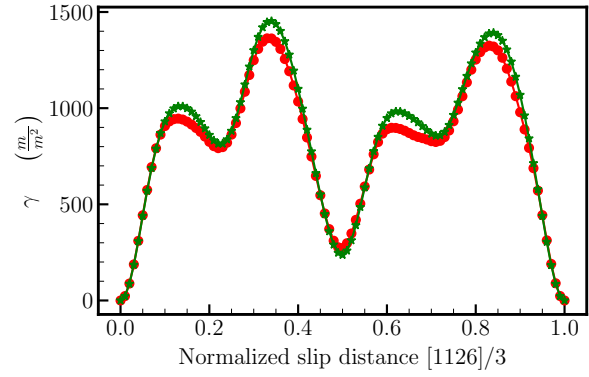
D. Potential Prediction

Being able to accurately model the Ti-Al system with varying concentrations of Al is very important. A potential must accurately display fundamental material properties with varying concentrations of Al as well as predict at what temperature or Al concentration phase changes will occur. Both RANN and MEAM [23] are capable of predicting the lattice constants as a function of varying Al concentration in agreement with the experimental works of Kornilov et al. [87] and Rostoker [88]. Lattice constants with varying aluminum temperature for MEAM at 0 K, RANN at 300 K, and experimental results at 300 K can be seen in Fig. 7. MEAM shows more accuracy in this regard; however, RANN replicates the experimental trend for the a-axis and approaches the experimental results with increasing Al concentration for the c-axis.

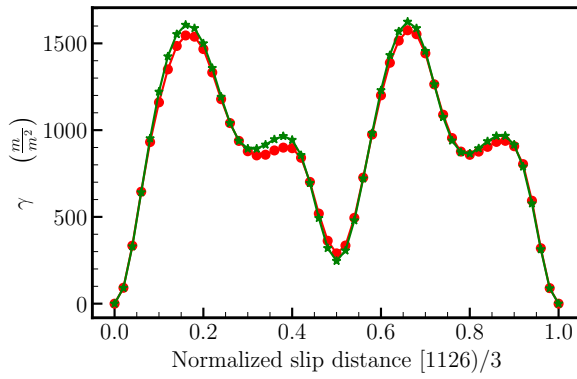
The RANN potential is capable of reproducing the phase diagram with up to 30% Al. The DO_{19} to α transition predicted by RANN is comparable to that of CALPHAD as well as previous work done by Kim et al. [23]. Simulations for this transition were run at 900



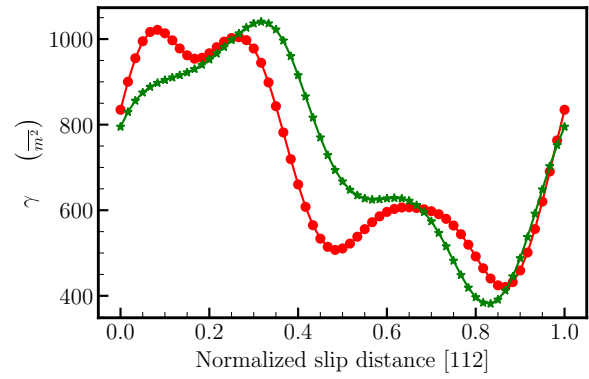
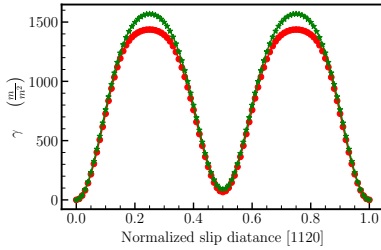
(a) Basal



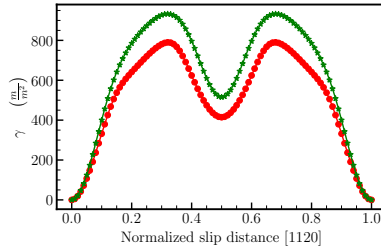
(b) Pyramidal I



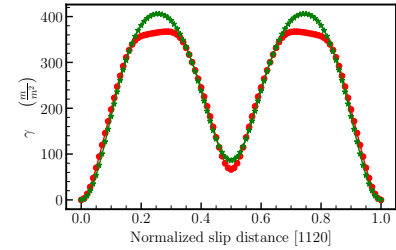
(c) Pyramidal II

(d) L1₀ (111)

(e) Prismatic Narrow



(f) Prismatic Wide I



(g) Prismatic Wide II

Figure 6. GSFE for (a-c,e-g) D0₁₉ (a) Basal, (b) Pyramidal I, (c) Pyramidal II, (d) L1₀ (111), (e) Prismatic Narrow, (f) Prismatic Wide I, (g) Prismatic Wide II planes.

K, 1000 K, 1100 K, and 1200 K. At temperatures higher than 1200 K the hysteresis loop becomes too small to accurately measure where the phase transition occurs. Fig. 8 shows the hysteresis loop found at 900 K.

RANN predicts the α to α +D0₁₉ phase boundary to occur at Al concentrations of 8.63%,

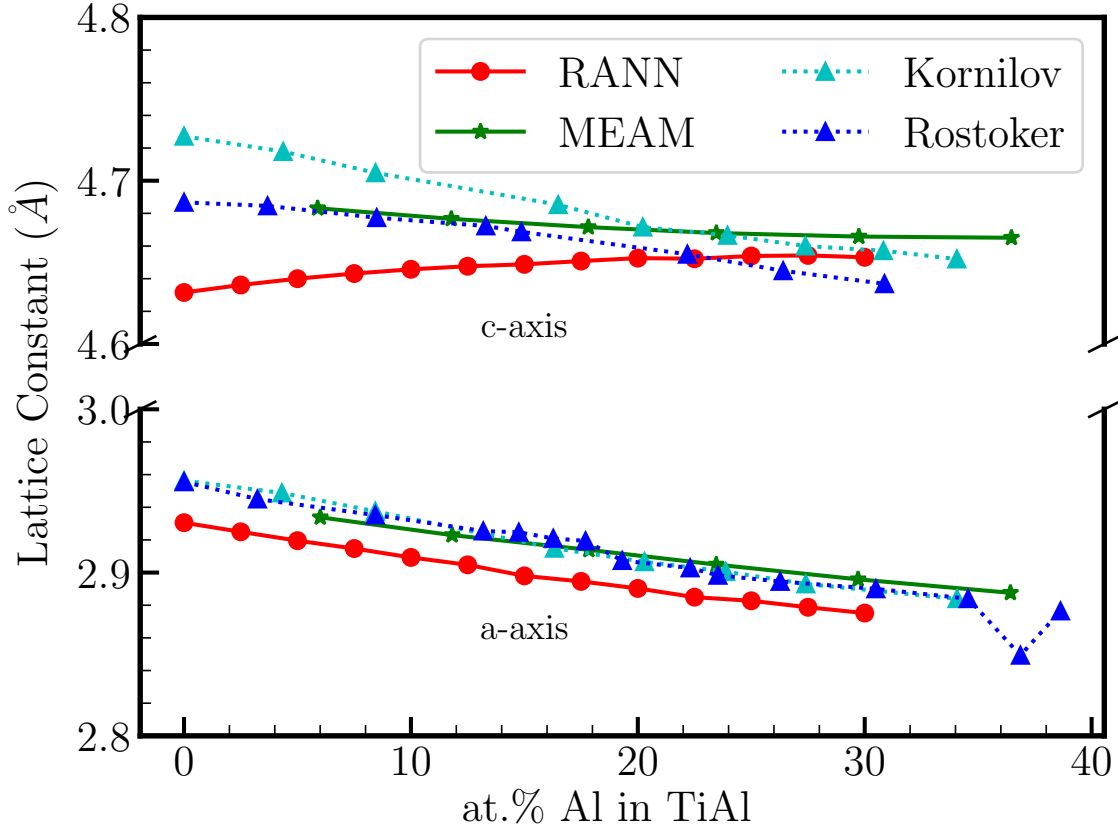
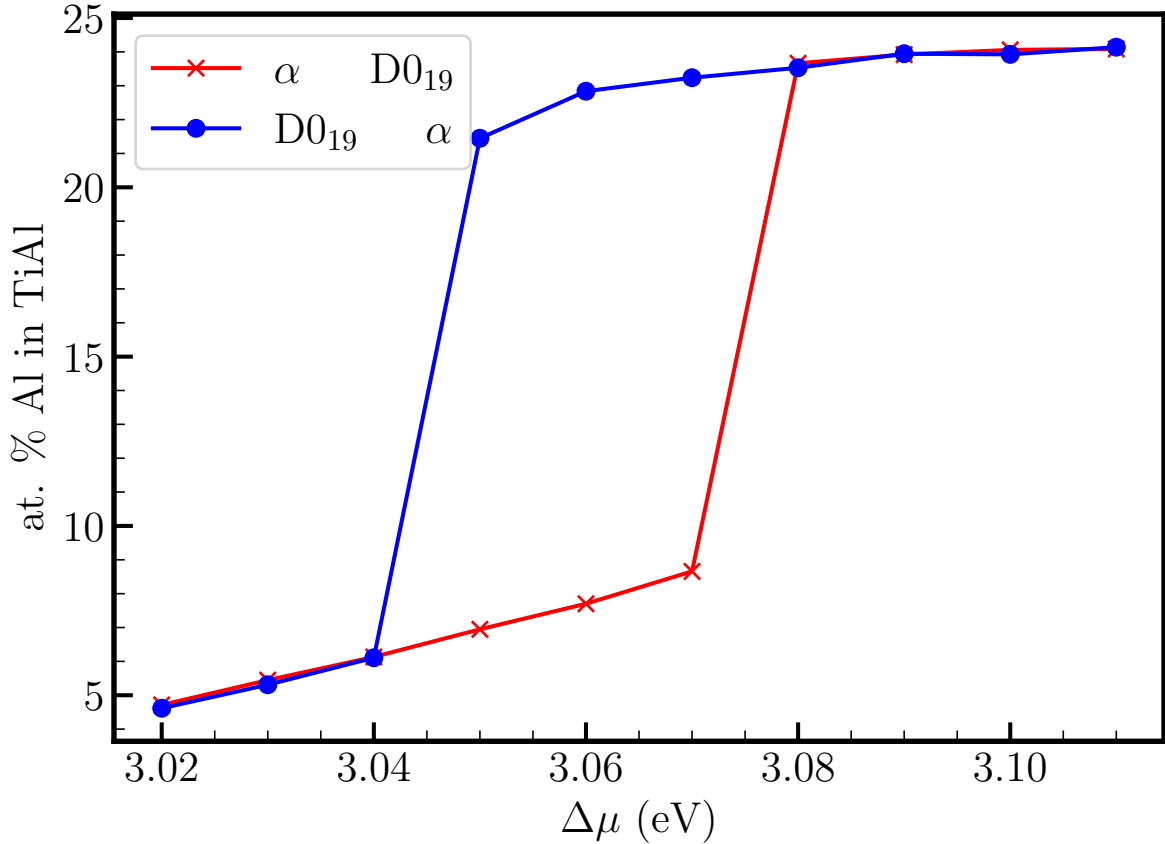


Figure 7. Lattice constant as a function of Al concentration for RANN (300 K), MEAM (0 K) [23], and experimental values (300 K) [87, 88].

9.66%, 11.10%, and 14.23% for temperatures of 900 K, 1000 K, 1100 K, and 1200 K, respectively. RANN predicts the $D0_{19}$ to $\alpha+D0_{19}$ phase boundary to be at Al concentrations of 22.72%, 22.25%, 21.57%, and 22.20% for the same temperatures. While MEAM [23] displays an accurate transition between α and $D0_{19}$, MTP [39] does not accurately predict this phase transition. MTP predicts a stable phase between the α and $D0_{19}$ phases and can be seen in the supplementary information [48].

To the best of the authors' knowledge, no existing interatomic potential exists that accurately shows Al as an α -stabilizer in Ti-Al alloys by reproducing the α to β transition. The ability to model this phase transition is of great importance as many commercially available Ti-Al alloys contain two-phase regions composed of the α and β phases in order to increase strength and creep resistance [89]. Additionally, the β phase is known to increase the workability of



(a) 900 K

Figure 8. Hysteresis loop from Semi-Grand-Canonical Monte Carlo Simulations at 900 K.

Ti alloys [90]. Fig. 9 displays the solid-liquid interface for the α and β phases at 10% Al concentration as well as the transition temperature for 0%, 10%, and 20% Al concentrations. Images used for the solid-liquid interface were taken from Ovito [91].

RANN predicts the α to β transition to be along the upper boundary of the two-phase region predicted by CALPHAD. The transition temperature was calculated for Al concentrations ranging from 0% Al to 20% Al in 2.5% increments.

In increasing order starting at 0% Al, the transition temperatures are found to be 1192 K, 1206 K, 1235 K, 1247 K, 1280 K, 1327 K, 1362 K, 1417 K, and 1427 K. These values show a clear trend of increasing transition temperature with increasing Al concentration as is expected when adding an α -stabilizer such as Al. The phase boundaries predicted by RANN are shown in Fig. 10.

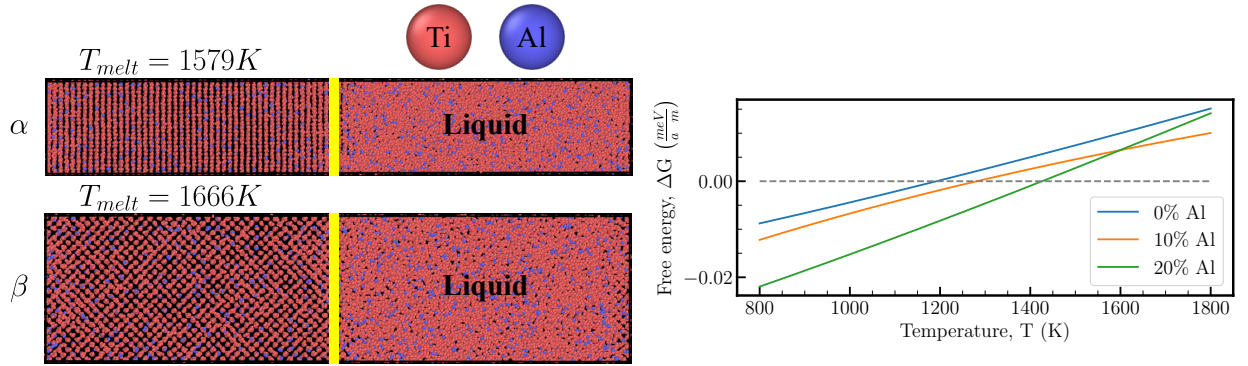


Figure 9. Left: solid-liquid interface for the α and β phases for 10% Al concentration [91]. Right: Gibbs free energy calculation for 0%, 10%, and 20% Al concentrations.

Table II. Melting temperatures used for calculation of the Gibbs relative free energy and α - β transition temperatures found from the Gibbs relative free energy.

at. % Al	T_{melt}^{α} (K)	T_{melt}^{β} (K)	$T_{transition}^{\alpha-\beta}$ (K)
0	1525.295	1657.246	1192.05
2.5	1522.220	1672.751	1205.65
5	1534.717	1674.698	1235.20
7.5	1561.384	1691.315	1246.50
10	1579.092	1665.697	1280.20
12.5	1592.222	1700.295	1326.95
15	1618.833	1706.940	1362.04
17.5	1620.266	1717.814	1417.22
20	1633.606	1737.773	1426.22

IV. DISCUSSION

The microstructure of Ti-Al alloys plays a key role in determining material properties. Previous attempts at modeling the Ti-Al system have been limited to only capturing solid solutions or formed intermetallics – not both. The RANN potential presented in this work bridges the gap between the currently available classical and ML potentials for the Ti-Al binary system. Classical potentials such as the MEAM potential introduced by Kim et al. [23] accurately model basic properties for solid solutions and formed intermetallic structures;

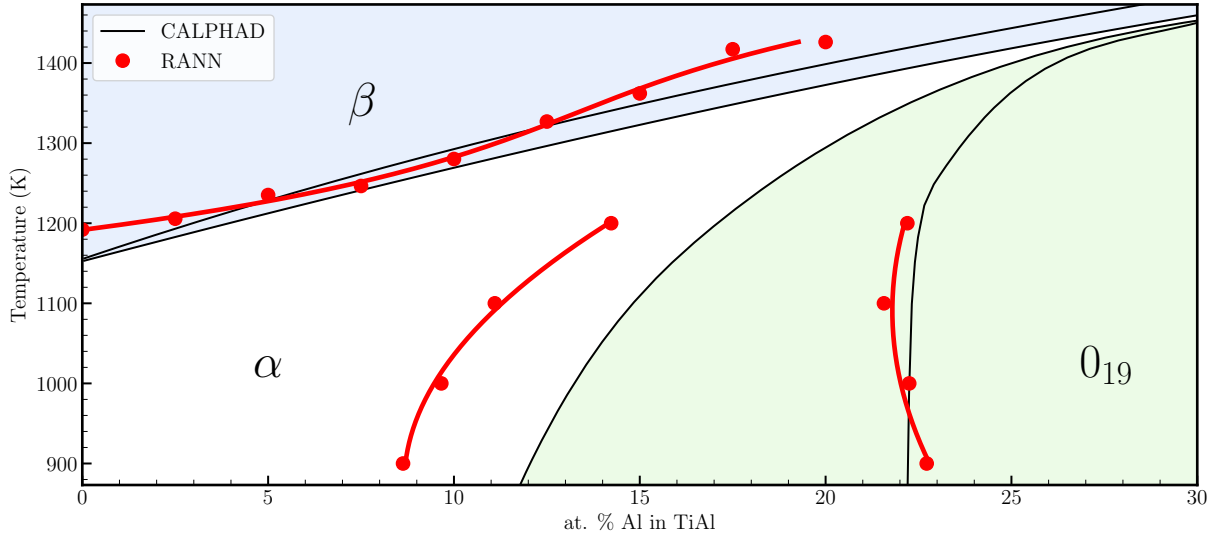


Figure 10. Phase diagram of Ti-Al binary system predicted by RANN compared to CALPHAD. The line between RANN data points is a cubic spline with an applied smoothing factor to indicate the trend of the data.

however, they fail to capture accurate GSFES and elastic constants for formed intermetallics. MEAM [23] also does not report on the α - β phase boundary. The MTP potential produced by Qi et al. [39] is promising for basic properties and plastic properties for formed intermetallic structures; however, it does not give accurate results for solid solutions. This ML potential also does not report on the α - β or α - O_{19} phase boundaries. The Ti-Al RANN potential gives basic properties and GSFES in agreement with DFT and phase boundaries in agreement with CALPHAD. The lattice constants and elastic constants predicted by RANN show an average deviation of 3.33% from DFT with the largest deviation coming from the C_{44} elastic constant for α -Ti. DFT shows a decrease in GSFE compared to α -Ti when adding an Al atom adjacent to the glide plane. RANN accurately displays this trend as well. RANN mimics the slope of the phase boundaries between α and β as well as α and O_{19} given by CALPHAD. The α to O_{19} phase boundary predicted by RANN occurs at an Al concentration roughly 3% lower than that of CALPHAD; however the O_{19} to α phase boundary given from RANN is within approximately 1% of CALPHAD. As the temperature increases in systems with an Al concentration near the α to O_{19} phase boundary, RANN correctly predicts that the α phase becomes more stable than the two-phase region containing α and

D0₁₉. RANN shows the α - β boundary to be along the upper phase boundary given by CALPHAD. This shows that the RANN potential accurately finds Al to be an α stabilizer when added to Ti. These results show that RANN is capable of modeling phase behaviors, solute effects, and thermomechanical properties of Ti-Al systems with up to 30% Al concentration. Furthermore, to the authors' knowledge, this is the only interatomic potential that is capable of reproducing the α - β phase boundary in the Ti-Al binary system.

REFERENCES

- [1] F. Appel, J. D. H. Paul, and M. Oehring, *Gamma titanium aluminide alloys: science and technology*. John Wiley & Sons, 2011.
- [2] H. Clemens and S. Mayer, “Intermetallic titanium aluminides in aerospace applications—processing, microstructure and properties,” *Materials at high temperatures*, vol. 33, no. 4-5, pp. 560–570, 2016.
- [3] C. Leyens and M. Peters, *Titanium and titanium alloys: fundamentals and applications*. Wiley Online Library, 2006.
- [4] D. Dimiduk, “Gamma titanium aluminide alloys—an assessment within the competition of aerospace structural materials,” *Materials Science and Engineering: A*, vol. 263, no. 2, pp. 281–288, 1999.
- [5] S.-W. Kim, Y.-S. Na, J.-T. Yeom, S. E. Kim, and Y. S. Choi, “An in-situ transmission electron microscopy study on room temperature ductility of tial alloys with fully lamellar microstructure,” *Materials Science and Engineering: A*, vol. 589, pp. 140–145, 2014.
- [6] A. J. Palomares-García, M. T. Pérez-Prado, and J. M. Molina-Aldareguia, “Effect of lamellar orientation on the strength and operating deformation mechanisms of fully lamellar tial alloys determined by micropillar compression,” *Acta Materialia*, vol. 123, pp. 102–114, 2017.
- [7] F. Appel and R. Wagner, “Microstructure and deformation of two-phase γ -titanium aluminides,” *Materials science and engineering: r: reports*, vol. 22, no. 5, pp. 187–268, 1998.
- [8] K. Jepson, A. R. Brown, and J. Gray, “Effect of cooling rate on the beta transformation in titanium–niobium and titanium–aluminium alloys.” Royal Aircraft Establishment, Farnborough, Eng., Tech. Rep., 1970.
- [9] T. Sato, S. Hukai, and Y. C. Huang, “The ms points of binary titanium alloys,” *J. Austral. Inst. Met.*, vol. 5, no. 2, pp. 149–149, 1960.
- [10] M. Asta, D. de Fontaine, M. van Schilfhaarde, M. Sluiter, and M. Methfessel, “First-principles phase-stability study of fcc alloys in the ti-al system,” *Physical Review B*, vol. 46, no. 9, p. 5055, 1992.
- [11] S. Shang, D. Kim, C. Zacherl, Y. Wang, Y. Du, and Z. Liu, “Effects of alloying elements and temperature on the elastic properties of dilute ni-base superalloys from first-principles calculations,” *Journal of Applied Physics*, vol. 112, no. 5, 2012.

- [12] Y. Liu, L. Liu, S. Wang, and H. Ye, "First-principles study of shear deformation in tial and ti3al," *Intermetallics*, vol. 15, no. 3, pp. 428–435, 2007.
- [13] R. Ding, H. Li, D. Hu, N. Martin, M. Dixon, and P. Bowen, "Features of fracture surface in a fully lamellar tial-base alloy," *Intermetallics*, vol. 58, pp. 36–42, 2015.
- [14] M. Yoo, J. Zou, and C. Fu, "Mechanistic modeling of deformation and fracture behavior in tial and ti3al," *Materials Science and Engineering: A*, vol. 192, pp. 14–23, 1995.
- [15] C. Fu and M. Yoo, "Elastic constants, fault energies, and dislocation reactions in tial: A first-principles total-energy investigation," *Philosophical Magazine Letters*, vol. 62, no. 3, pp. 159–165, 1990.
- [16] J. Sun, P. Trimby, X. Si, X. Liao, N. Tao, and J. Wang, "Nano twins in ultrafine-grained ti processed by dynamic plastic deformation," *Scripta Materialia*, vol. 68, no. 7, pp. 475–478, 2013.
- [17] T. Lee, S.-W. Kim, J. Y. Kim, W.-S. Ko, and S. Ryu, "First-principles study of the ternary effects on the plasticity of γ -tial crystals," *Scientific Reports*, vol. 10, no. 1, p. 21614, 2020.
- [18] M. S. Daw and M. I. Baskes, "Embedded-atom method: Derivation and application to impurities, surfaces, and other defects in metals," *Physical Review B*, vol. 29, no. 12, p. 6443, 1984.
- [19] D. Farkas and C. Jones, "Interatomic potentials for ternary nb-ti-al alloys," *Modelling and Simulation in Materials Science and Engineering*, vol. 4, no. 1, p. 23, 1996.
- [20] R. R. Zope and Y. Mishin, "Interatomic potentials for atomistic simulations of the ti-al system," *Physical Review B*, vol. 68, no. 2, p. 024102, 2003.
- [21] M. Baskes, "Application of the embedded-atom method to covalent materials: a semiempirical potential for silicon," *Physical review letters*, vol. 59, no. 23, p. 2666, 1987.
- [22] M. Baskes, J. Nelson, and A. Wright, "Semiempirical modified embedded-atom potentials for silicon and germanium," *Physical Review B*, vol. 40, no. 9, p. 6085, 1989.
- [23] Y.-K. Kim, H.-K. Kim, W.-S. Jung, and B.-J. Lee, "Atomistic modeling of the ti-al binary system," *Computational materials science*, vol. 119, pp. 1–8, 2016.
- [24] Y. Koizumi, S. Ogata, Y. Minamino, and N. Tsuji, "Energies of conservative and non-conservative antiphase boundaries in ti3al: a first principles study," *Philosophical Magazine*, vol. 86, no. 9, pp. 1243–1259, 2006.

- [25] L. Karkina and L. Yakovenkova, "Dislocation core structure and deformation behavior of Ti_3Al ," *Modelling and Simulation in Materials Science and Engineering*, vol. 20, no. 6, p. 065003, 2012.
- [26] M. Legros, A. Corn, and D. Caillard, "Prismatic and basal slip in Ti_3Al i. frictional forces on dislocations," *Philosophical Magazine A*, vol. 73, no. 1, pp. 61–80, 1996.
- [27] Q.-X. Pei, M. Jhon, S. S. Quek, and Z. Wu, "A systematic study of interatomic potentials for mechanical behaviours of Ti-Al alloys," *Computational Materials Science*, vol. 188, p. 110239, 2021.
- [28] J. S. Smith, O. Isayev, and A. E. Roitberg, "Ani-1: an extensible neural network potential with dft accuracy at force field computational cost," *Chemical science*, vol. 8, no. 4, pp. 3192–3203, 2017.
- [29] J. A. Vita and D. R. Trinkle, "Spline-based neural network interatomic potentials: Blending classical and machine learning models," *Computational Materials Science*, vol. 232, p. 112655, 2024.
- [30] T. Morawietz and N. Artrith, "Machine learning-accelerated quantum mechanics-based atomistic simulations for industrial applications," *Journal of Computer-Aided Molecular Design*, vol. 35, no. 4, pp. 557–586, 2021.
- [31] Y. Zuo, C. Chen, X. Li, Z. Deng, Y. Chen, J. Behler, G. Csányi, A. V. Shapeev, A. P. Thompson, M. A. Wood *et al.*, "Performance and cost assessment of machine learning interatomic potentials," *The Journal of Physical Chemistry A*, vol. 124, no. 4, pp. 731–745, 2020.
- [32] V. L. Deringer, M. A. Caro, and G. Csányi, "Machine learning interatomic potentials as emerging tools for materials science," *Advanced Materials*, vol. 31, no. 46, p. 1902765, 2019.
- [33] J. Behler, "Perspective: Machine learning potentials for atomistic simulations," *The Journal of chemical physics*, vol. 145, no. 17, 2016.
- [34] R. Kobayashi, D. Giofré, T. Junge, M. Ceriotti, and W. A. Curtin, "Neural network potential for Al-Mg-Si alloys," *Physical Review Materials*, vol. 1, no. 5, p. 053604, 2017.
- [35] D. Dickel, M. Nitol, and C. Barrett, "Lammps implementation of rapid artificial neural network derived interatomic potentials," *Computational Materials Science*, vol. 196, p. 110481, 2021.
- [36] A. P. Thompson, L. P. Swiler, C. R. Trott, S. M. Foiles, and G. J. Tucker, "Spectral neighbor analysis method for automated generation of quantum-accurate interatomic potentials,"

- Journal of Computational Physics*, vol. 285, pp. 316–330, 2015.
- [37] A. P. Bartók, M. C. Payne, R. Kondor, and G. Csányi, “Gaussian approximation potentials: The accuracy of quantum mechanics, without the electrons,” *Physical review letters*, vol. 104, no. 13, p. 136403, 2010.
- [38] A. V. Shapeev, “Moment tensor potentials: A class of systematically improvable interatomic potentials,” *Multiscale Modeling & Simulation*, vol. 14, no. 3, pp. 1153–1173, 2016.
- [39] J. Qi, Z. Aitken, Q. Pei, A. M. Z. Tan, Y. Zuo, M. Jhon, S. Quek, T. Wen, Z. Wu, and S. P. Ong, “Machine learning moment tensor potential for modelling dislocation and fracture in $\text{Ti}_{10}\text{-TiAl}$ and $\text{d}_{019}\text{-Ti}_{3}\text{Al}$ alloys,” *arXiv preprint arXiv:2305.11825*, 2023.
- [40] A. Seko, “Machine learning potentials for multicomponent systems: The Ti-Al binary system,” *Physical Review B*, vol. 102, no. 17, p. 174104, 2020.
- [41] D. Dickel, C. D. Barrett, R. L. Carino, M. I. Baskes, and M. F. Horstemeyer, “Mechanical instabilities in the modeling of phase transitions of titanium,” *Modelling and Simulation in Materials Science and Engineering*, vol. 26, no. 6, p. 065002, 2018.
- [42] M. S. Nitol, D. E. Dickel, and C. D. Barrett, “Machine learning models for predictive materials science from fundamental physics: An application to titanium and zirconium,” *Acta Materialia*, vol. 224, p. 117347, 2022.
- [43] M. S. Nitol, K. Dang, S. J. Fensin, M. I. Baskes, D. E. Dickel, and C. D. Barrett, “Hybrid interatomic potential for Sn,” *Phys. Rev. Mater.*, vol. 7, p. 043601, Apr 2023. [Online]. Available: <https://link.aps.org/doi/10.1103/PhysRevMaterials.7.043601>
- [44] M. S. Nitol, S. Mun, D. E. Dickel, and C. D. Barrett, “Unraveling Mg-Cu slip using neural network potential,” *Philosophical Magazine*, vol. 102, no. 8, pp. 651–673, 2022.
- [45] M. S. Nitol, D. E. Dickel, and C. D. Barrett, “Artificial neural network potential for pure zinc,” *Computational Materials Science*, vol. 188, p. 110207, 2021.
- [46] J. Hafner, “Ab-initio simulations of materials using vasp: Density-functional theory and beyond,” *Journal of computational chemistry*, vol. 29, no. 13, pp. 2044–2078, 2008.
- [47] J. P. Perdew, K. Burke, and M. Ernzerhof, “Generalized gradient approximation made simple,” *Physical review letters*, vol. 77, no. 18, p. 3865, 1996.
- [48] See Supplemental Material at URL-will-be-inserted-by-publisher for information on DFT database; RANN, DFT, and experimental values for material properties; and testing with other potentials.

- [49] D. Dickel, D. Francis, and C. Barrett, “Neural network aided development of a semi-empirical interatomic potential for titanium,” *Computational Materials Science*, vol. 171, p. 109157, 2020.
- [50] M. I. Baskes, “Determination of modified embedded atom method parameters for nickel,” *Materials Chemistry and Physics*, vol. 50, no. 2, pp. 152–158, 1997.
- [51] B.-J. Lee and M. I. Baskes, “Second nearest-neighbor modified embedded-atom-method potential,” *Physical Review B*, vol. 62, no. 13, p. 8564, 2000.
- [52] K. Levenberg, “A method for the solution of certain non-linear problems in least squares,” *Quarterly of applied mathematics*, vol. 2, no. 2, pp. 164–168, 1944.
- [53] D. W. Marquardt, “An algorithm for least-squares estimation of nonlinear parameters,” *Journal of the society for Industrial and Applied Mathematics*, vol. 11, no. 2, pp. 431–441, 1963.
- [54] N. Artrith and A. Urban, “An implementation of artificial neural-network potentials for atomistic materials simulations: Performance for tio₂,” *Computational Materials Science*, vol. 114, pp. 135–150, 2016.
- [55] C. A. Becker, F. Tavazza, Z. T. Trautt, and R. A. Buarque de Macedo, “Considerations for choosing and using force fields and interatomic potentials in materials science and engineering,” *Current Opinion in Solid State and Materials Science*, vol. 17, no. 6, pp. 277–283, 2013, frontiers in Methods for Materials Simulations. [Online]. Available: <https://www.sciencedirect.com/science/article/pii/S1359028613000788>
- [56] L. M. Hale, Z. T. Trautt, and C. A. Becker, “Evaluating variability with atomistic simulations: the effect of potential and calculation methodology on the modeling of lattice and elastic constants,” *Modelling and Simulation in Materials Science and Engineering*, vol. 26, no. 5, p. 055003, may 2018. [Online]. Available: <https://dx.doi.org/10.1088/1361-651X/aabc05>
- [57] B. Sadigh, P. Erhart, A. Stukowski, A. Caro, E. Martinez, and L. Zepeda-Ruiz, “Scalable parallel monte carlo algorithm for atomistic simulations of precipitation in alloys,” *Physical Review B*, vol. 85, no. 18, p. 184203, 2012.
- [58] N. Metropolis, A. W. Rosenbluth, M. N. Rosenbluth, A. H. Teller, and E. Teller, “Equation of state calculations by fast computing machines,” *The journal of chemical physics*, vol. 21, no. 6, pp. 1087–1092, 1953.
- [59] G. Simmons and H. Wang, “Single crystal elastic constants and calculated aggregate properties: a handbook,” (*No Title*), 1971.

- [60] B. Yin, Z. Wu, and W. Curtin, “Comprehensive first-principles study of stable stacking faults in hcp metals,” *Acta Materialia*, vol. 123, pp. 223–234, 2017.
- [61] C. Kittel, *Introduction to solid state physics*. John Wiley & sons, inc, 2005.
- [62] E. Fisher and C. Renken, “Single-crystal elastic moduli and the hcp→ bcc transformation in ti, zr, and hf,” *Physical review*, vol. 135, no. 2A, p. A482, 1964.
- [63] F. R. Boer, *Cohesion in metals: transition metal alloys*. North Holland, 1988, vol. 1.
- [64] W. Tyson and W. Miller, “Surface free energies of solid metals: Estimation from liquid surface tension measurements,” *Surface Science*, vol. 62, no. 1, pp. 267–276, 1977.
- [65] J. S. Blakemore, *Solid state physics*. Cambridge university press, 1985.
- [66] C. Malica and A. Dal Corso, “Quasi-harmonic temperature dependent elastic constants: applications to silicon, aluminum, and silver,” *Journal of Physics: Condensed Matter*, vol. 32, no. 31, p. 315902, 2020.
- [67] W. Li and T. Wang, “Ab initio investigation of the elasticity and stability of aluminium,” *Journal of Physics: Condensed Matter*, vol. 10, no. 43, p. 9889, 1998.
- [68] H. Wang and M. Li, “Ab initio calculations of second-, third-, and fourth-order elastic constants for single crystals,” *Physical review B*, vol. 79, no. 22, p. 224102, 2009.
- [69] R. Golesorkhtabar, P. Pavone, J. Spitaler, P. Puschnig, and C. Draxl, “Elastic: A tool for calculating second-order elastic constants from first principles,” *Computer Physics Communications*, vol. 184, no. 8, pp. 1861–1873, 2013.
- [70] S. Shang, A. Saengdeejing, Z. Mei, D. Kim, H. Zhang, S. Ganeshan, Y. Wang, and Z. Liu, “First-principles calculations of pure elements: Equations of state and elastic stiffness constants,” *Computational Materials Science*, vol. 48, no. 4, pp. 813–826, 2010.
- [71] G. Lu, N. Kioussis, V. V. Bulatov, and E. Kaxiras, “Generalized-stacking-fault energy surface and dislocation properties of aluminum,” *Physical Review B*, vol. 62, no. 5, p. 3099, 2000.
- [72] X.-Z. Wu, R. Wang, S.-F. Wang, and Q.-Y. Wei, “Ab initio calculations of generalized-stacking-fault energy surfaces and surface energies for fcc metals,” *Applied Surface Science*, vol. 256, no. 21, pp. 6345–6349, 2010.
- [73] R. Smallman and P. Dobson, “Stacking fault energy measurement from diffusion,” *Metallurgical Transactions*, vol. 1, pp. 2383–2389, 1970.
- [74] C. Woodward, D. Trinkle, L. Hector Jr, and D. Olmsted, “Prediction of dislocation cores in aluminum from density functional theory,” *Physical review letters*, vol. 100, no. 4, p. 045507,

- 2008.
- [75] S. Crampin, K. Hampel, D. Vvedensky, and J. MacLaren, “The calculation of stacking fault energies in close-packed metals,” *Journal of Materials Research*, vol. 5, pp. 2107–2119, 1990.
- [76] P. Denteneer and J. Soler, “Defect energetics in aluminium,” *Journal of Physics: Condensed Matter*, vol. 3, no. 45, p. 8777, 1991.
- [77] B. Hammer, K. Jacobsen, V. Milman, and M. Payne, “Stacking fault energies in aluminium,” *Journal of Physics: Condensed Matter*, vol. 4, no. 50, p. 10453, 1992.
- [78] T. Hehenkamp, “Absolute vacancy concentrations in noble metals and some of their alloys,” *Journal of Physics and Chemistry of Solids*, vol. 55, no. 10, pp. 907–915, 1994.
- [79] K. Tanaka, K. Okamoto, H. Inui, Y. Minonishi, M. Yamaguchi, and M. Koiwa, “Elastic constants and their temperature dependence for the intermetallic compound Ti_3Al ,” *Philosophical Magazine A*, vol. 73, no. 5, pp. 1475–1488, 1996.
- [80] Y. Wei, Y. Zhang, G.-H. Lu, and H. Xu, “Site preference and elastic properties of a 2-ti 3 al with oxygen impurity: A first-principles study,” *International Journal of Modern Physics B*, vol. 24, no. 15n16, pp. 2749–2755, 2010.
- [81] C. Zhang, H. Hou, Y. Zhao, X. Yang, and Y. Guo, “First-principles study on structural, elastic and thermal properties of γ -tial and α_2 - Ti_3Al phases in tial-based alloy under high pressure,” *International Journal of Modern Physics B*, vol. 31, no. 11, p. 1750079, 2017.
- [82] W. B. Pearson, *A handbook of lattice spacings and structures of metals and alloys: International series of monographs on metal physics and physical metallurgy, Vol. 4*. Elsevier, 2013, vol. 4.
- [83] K. Tanaka, “Single-crystal elastic constants of γ -tial,” *Philosophical magazine letters*, vol. 73, no. 2, pp. 71–78, 1996.
- [84] H. Fu, Z. Zhao, W. Liu, F. Peng, T. Gao, and X. Cheng, “Ab initio calculations of elastic constants and thermodynamic properties of γ tial under high pressures,” *Intermetallics*, vol. 18, no. 5, pp. 761–766, 2010.
- [85] P. Kwasniak, H. Garbacz, and K. Kurzydowski, “Solid solution strengthening of hexagonal titanium alloys: Restoring forces and stacking faults calculated from first principles,” *Acta Materialia*, vol. 102, pp. 304–314, 2016.
- [86] S. Rao, A. Venkateswaran, and M. Letherwood, “Molecular statics and molecular dynamics simulations of the critical stress for motion of $a/3(1120)$ screw dislocations in α -ti at low

- temperatures using a modified embedded atom method potential,” *Acta materialia*, vol. 61, no. 6, pp. 1904–1912, 2013.
- [87] I. Kornilov, E. Pylaeva, and M. Volkova, “Phase diagram of the binary system titanium-aluminum,” *Bulletin of the Academy of Sciences of the USSR, Division of chemical science*, vol. 5, pp. 787–795, 1956.
- [88] W. Rostoker, “Observations on the lattice parameters of the alpha solid solution in the titanium-aluminum system,” *Jom*, vol. 4, no. 2, pp. 212–213, 1952.
- [89] R. Hennig, T. Lenosky, D. Trinkle, S. Rudin, and J. Wilkins, “Classical potential describes martensitic phase transformations between the α , β , and ω titanium phases,” *Physical Review B*, vol. 78, no. 5, p. 054121, 2008.
- [90] C. Veiga, J. P. Davim, and A. Loureiro, “Properties and applications of titanium alloys: a brief review,” *Rev. Adv. Mater. Sci*, vol. 32, no. 2, pp. 133–148, 2012.
- [91] A. Stukowski, “Visualization and analysis of atomistic simulation data with OVITO-the Open Visualization Tool,” *MODELLING AND SIMULATION IN MATERIALS SCIENCE AND ENGINEERING*, vol. 18, no. 1, JAN 2010.

Predicting Ti-Al Binary Phase Diagram with an Artificial Neural Network Potential - Supplemental Information

Micah Nichols, Christopher D. Barrett, and Doyl E. Dickel*

*Michael W. Hall School of Mechanical Engineering and
Center for Advanced Vehicular Systems, Mississippi State University,
Mississippi State, Mississippi 39762, USA*

Mashroor S. Nitol and Saryu J. Fensin

Los Alamos National Laboratory, Los Alamos, NM, 87545, USA

* doyl@me.msstate.edu

I. DFT TRAINING DATABASE

The DFT training database contains 69,558 simulations with 3,140,478 unique atomic environments. Simulations can be broken down into those that use bulk structures and those that use structures with defects. Both of these groups contain structures of pure Ti, pure Al, and Ti-Al. Bulk structures are pristine crystalline structures that are strained and undergo thermal perturbation. Simulations for bulk structures can be found in [Table I](#). Defect structures contain interstitials, vacancies, dislocation cores, or other imperfections within the crystal lattice. For the purpose of this database, amorphous data is also considered a defect structure. Information on defect structures in the DFT database can be found in [Table II](#).

Table I. DFT database of bulk structures used for features in input layers of the RANN potential.

Sample description	Atoms per simulation	Number of simulations	Total atomic environment
α -Ti w/ volumetric strains up to $\pm 20\%$	2	99	198
β -Ti w/ volumetric strains up to $\pm 20\%$	2	99	198
ω -Ti w/ volumetric strains up to $\pm 20\%$	3	99	297
$a15$ -Ti w/ volumetric strains up to $\pm 20\%$	8	99	792
DC -Ti w/ volumetric strains up to $\pm 20\%$	8	99	792
FCC -Ti w/ volumetric strains up to $\pm 20\%$	4	99	396
sc -Ti w/ volumetric strains up to $\pm 20\%$	1	99	99
FCC -Al w/ volumetric strains up to $\pm 20\%$	2	99	198
ω -Al w/ volumetric strains up to $\pm 20\%$	3	99	297
α -Ti w/ shear strains up to $\pm 5\%$	2	1386	2772
β -Ti w/ shear strains up to $\pm 5\%$	2	1386	2772
ω -Ti w/ shear strains up to $\pm 5\%$	3	1386	4158
FCC -Al w/ shear strains up to $\pm 5\%$	2	1386	2772
Ti_3Al (DO_{19}) w/ shear strains up to $\pm 5\%$	8	1386	10848
$TiAl$ ($L1_0$) w/ shear strains up to $\pm 5\%$	4	1256	5024
FCC -Al w/ shear strains up to $\pm 5\%$	2	1386	2772
α - Ti $3 \times 3 \times 3$ orthogonal supercell w/ strains up to $\pm 5\%$	54	961	51894
β - Ti $3 \times 3 \times 3$ orthogonal supercell w/ strains up to $\pm 5\%$	54	1000	54000
ω - Ti $3 \times 3 \times 3$ orthogonal supercell w/ strains up to $\pm 5\%$	81	783	63423
FCC - Ti $3 \times 3 \times 3$ orthogonal supercell w/ strains up to $\pm 5\%$	32	300	9600
FCC - Al $3 \times 3 \times 3$ orthogonal supercell w/ strains up to $\pm 5\%$	54	995	53730
FCC - Al $3 \times 3 \times 3$ orthogonal supercell w/ strains up to $\pm 5\%$	32	299	9568
HCP - Al $3 \times 3 \times 3$ orthogonal supercell w/ strains up to $\pm 5\%$	54	135	7290
ω - Al $2 \times 2 \times 3$ orthogonal supercell w/ strains up to $\pm 5\%$	36	199	7164
Ti_3Al (DO_{19}) $2 \times 2 \times 2$ orthogonal supercell w/ strains up to $\pm 5\%$	64	500	38336
$TiAl(L1_0)$ $2 \times 2 \times 2$ orthogonal supercell w/ strains up to $\pm 5\%$	32	500	16000
$TiAl_3$ (DO_{22}) $2 \times 2 \times 2$ orthogonal supercell w/ strains up to $\pm 5\%$	64	500	38336
$TiAl_2$ (Ga_2Hf) $2 \times 2 \times 1$ orthogonal supercell w/ strains up to $\pm 5\%$	96	500	48000
$TiAl(B2)$ $2 \times 2 \times 2$ orthogonal supercell w/ strains up to $\pm 5\%$	108	293	31644
β - Ti + $Al(1 - 50\%)$ $3 \times 3 \times 3$ orthogonal supercell w/ strains up to $\pm 5\%$	54	1636	88344
α - Ti + $Al(1 - 50\%)$ $3 \times 3 \times 3$ orthogonal supercell w/ strains up to $\pm 5\%$	54	1899	102546
ω - Ti + $Al(1 - 50\%)$ $3 \times 3 \times 2$ orthogonal supercell w/ strains up to $\pm 5\%$	54	966	53784
FCC - Ti + $Al(1 - 50\%)$ $2 \times 2 \times 2$ orthogonal supercell w/ strains up to $\pm 5\%$	32	762	24384
FCC - Al + $Ti(1 - 50\%)$ $2 \times 2 \times 2$ orthogonal supercell w/ strains up to $\pm 5\%$	32	1799	57568
HCP - Al + $Ti(1 - 50\%)$ $3 \times 3 \times 3$ orthogonal supercell w/ strains up to $\pm 5\%$	54	852	46008

Table II. DFT database of defects used for features in input layers of the RANN potential.

Sample description	Atoms per simulation	Number of simulations	Total atomic environment
$\alpha - Ti$ (1 Octahedral interstitial) $3 \times 3 \times 3$ orthogonal supercell w/ strains up to $\pm 5\%$	55	89	4895
$\beta - Ti$ (1 Octahedral interstitial) $3 \times 3 \times 3$ orthogonal supercell w/ strains up to $\pm 5\%$	55	201	11055
$FCC - Al$ (1 Octahedral interstitial) $3 \times 3 \times 3$ orthogonal supercell w/ strains up to $\pm 5\%$	55	201	11055
$\alpha - Ti$ (1 Octahedral interstitial)+ $Al:1 - 50\%$) $3 \times 3 \times 3$ orthogonal supercell w/ strains up to $\pm 5\%$	55	420	23100
$\beta - Ti$ (1 Octahedral interstitial)+ $Al:1 - 50\%$) $3 \times 3 \times 3$ orthogonal supercell w/ strains up to $\pm 5\%$	55	1200	66000
$FCC - Al$ (1 Octahedral interstitial)+ $Ti:1 - 50\%$) $2 \times 2 \times 2$ orthogonal supercell w/ strains up to $\pm 5\%$	33	1129	37257
$\alpha - Ti$ (1 Tetrahedral interstitial) $3 \times 3 \times 3$ orthogonal supercell w/ strains up to $\pm 5\%$	55	199	10945
$\beta - Ti$ (1 Tetrahedral interstitial) $3 \times 3 \times 3$ orthogonal supercell w/ strains up to $\pm 5\%$	55	201	11055
$FCC - Al$ (1 Tetrahedral interstitial) $3 \times 3 \times 3$ orthogonal supercell w/ strains up to $\pm 5\%$	33	201	6633
$\beta - Ti$ (1 Tetrahedral interstitial)+ $Al:1 - 50\%$) $3 \times 3 \times 3$ orthogonal supercell w/ strains up to $\pm 5\%$	55	1198	65890
$FCC - Al$ (1 Tetrahedral interstitial)+ $Ti:1 - 50\%$) $3 \times 3 \times 3$ orthogonal supercell w/ strains up to $\pm 5\%$	33	1200	39600
$\alpha - Ti$ (Mono vacancy) $3 \times 3 \times 3$ orthogonal supercell w/ strains up to $\pm 5\%$	53	117	6201
$\beta - Ti$ (Mono vacancy) $3 \times 3 \times 3$ orthogonal supercell w/ strains up to $\pm 5\%$	53	200	10600
$\omega - Ti$ (Mono vacancy) $2 \times 2 \times 3$ orthogonal supercell w/ strains up to $\pm 5\%$	53	106	5618
$FCC - Al$ (Mono vacancy) $3 \times 3 \times 3$ orthogonal supercell w/ strains up to $\pm 5\%$	31	200	6200
$\alpha - Ti$ (Mono vacancy)+ $Al:1 - 50\%$) $3 \times 3 \times 3$ orthogonal supercell w/ strains up to $\pm 5\%$	53	550	29150
$\beta - Ti$ (Mono vacancy)+ $Al:1 - 50\%$) $3 \times 3 \times 3$ orthogonal supercell w/ strains up to $\pm 5\%$	53	1200	63600
$FCC - Al$ (Mono vacancy)+ $Ti:1 - 50\%$) $3 \times 3 \times 3$ orthogonal supercell w/ strains up to $\pm 5\%$	33	1180	38940
$\alpha - Ti$ ([000 1],[1 1 0 0], [1 2 1 0]) monolayer orthogonal supercell w/ strains up to $\pm 5\%$	(32-36)	580	16120
$\beta - Ti$ ([1 1 0],[1 1 0],[1 1 2]) monolayer orthogonal supercell w/ strains up to $\pm 5\%$	(32-48)	590	23600
$\omega - Ti$ ([000 1]) monolayer orthogonal supercell w/ strains up to $\pm 5\%$	36	200	7200
$FCC - Al$ ([1 1 0],[1 1 0],[1 1 2]) monolayer orthogonal supercell w/ strains up to $\pm 5\%$	(32-48)	346	11764
$\alpha - Ti$ ([000 1],[1 1 0 0], [1 2 1 0])+ $Al:1 - 25\%$) monolayer orthogonal supercell w/ strains up to $\pm 5\%$	(32-36)	983	33422
$\beta - Ti$ ([1 1 0],[1 1 0],[1 1 2])+ $Al:1 - 25\%$) monolayer orthogonal supercell w/ strains up to $\pm 5\%$	(32-48)	882	35280
$\omega - Ti$ ([000 1])+ $Al:1 - 25\%$) monolayer orthogonal supercell w/ strains up to $\pm 5\%$	36	352	12672
$FCC - Al$ ([1 1 0],[1 1 0],[1 1 2])+ $Ti:1 - 25\%$) monolayer orthogonal supercell w/ strains up to $\pm 5\%$	(32-48)	724	24616
$\alpha - Ti$ ([000 1],[1 1 0 0],[1 1 2 0]) separation distance	(16-48)	200	6400
$FCC - Al$ ([1 1 0],[1 1 0],[1 2 3]) separation distance	(12-36)	200	4800
$\alpha - Ti$ dislocation core structure (prismatic,prismatic-saddle,pyramidal, pyramidal-saddle)	192	80	15360
Amorphous structure : Ti	(40-43)	200	8300
Amorphous structure : Al	(55-62)	200	11700
Amorphous structure : $Ti - Al(1 - 50\%)$	(66-95)	200	57892
Isolate atom	2	1	2

II. TI

The values for the material properties of the α , β , and ω phases of pure Ti from experiments, DFT, and RANN at 0 K can be seen in [Table III](#). This table shows that the Ti-Al RANN potential gives results near the accuracy of DFT.

Table III. Pure Ti properties: *italic* are from previous DFT. a and c - lattice constants, E_c - cohesive energy, B - the bulk modulus, C - elastic constants, ΔE - structural energy difference, $E_{surface}$ - surface energy, E^{vac} - vacancy formation energy, E^{inter} - interstitial energy. Experimental results for the β phase are at finite temperature.

Properties	α		β		ω	
	Expt./DFT	RANN	Expt./DFT	RANN	DFT	RANN
a (\AA)	2.947 ^a / <i>2.92^b</i> , 2.92	2.93	<i>3.26^c</i> , 3.24	3.24	4.55	4.53
c (\AA)	4.686 ^a / <i>4.63^b</i> , 4.63	4.61			2.82	2.83
c/a ratio	1.586 ^a / <i>1.58^b</i> , 1.58	1.58			0.62	0.62
E_c (eV)	4.85 ^d / <i>5.32</i>	3.23	5.22	3.13	5.31	3.24
B (GPa)		117.59		110.93		115.73
C_{11} (GPa)	176.1 ^a / <i>177^b</i> , 176.6	170.41	134 ^e / <i>89^c</i> , 93.51	124.36	<i>198^c</i> , 193.15	178.29
C_{12} (GPa)	86.9 ^a / <i>90^b</i> , 91.6	91.45	110 ^e / <i>112^c</i> , 114.6	108.63	<i>84^c</i> , 86	112.87
C_{13} (GPa)	68.3 ^a / <i>84^b</i> , 84.2	83.56			<i>53^c</i> , 54	79.65
C_{33} (GPa)	190.5 ^a / <i>189^b</i> , 192.2	197.19			<i>246^c</i> , 248	206.35
C_{44} (GPa)	50.8 ^a / <i>40^b</i> , 40.72	47.75	36 ^e / <i>42^c</i> , 40.19	44.53	<i>54^c</i> , 54	65.97
$\Delta E_{hcp \rightarrow bcc}$ ($\frac{eV}{atom}$)	/0.10	0.10				
$\Delta E_{hcp \rightarrow fcc}$ ($\frac{eV}{atom}$)	/0.06	0.06				
$\Delta E_{hcp \rightarrow sc}$ ($\frac{eV}{atom}$)	/0.79	0.79				
$\Delta E_{hcp \rightarrow a15}$ ($\frac{eV}{atom}$)	/0.18	0.18				
$\Delta E_{hcp \rightarrow dc}$ ($\frac{eV}{atom}$)	/2.266	1.95				
$\Delta E_{hcp \rightarrow \omega}$ ($\frac{eV}{atom}$)	/-0.01	-0.01				
$E_{surface}^{(0001)}$ ($\frac{mJ}{m^2}$)	2.1 ^f / <i>1.95</i>	1.93				
$E_{surface}^{(1010)}$ ($\frac{mJ}{m^2}$)	1.92 ^g / <i>2.00</i>	2.01				
E_f^{vac} (eV)	/2.03	2.04				
E_{octa}^{inter} (eV)	/2.59	2.62				
$E_{Dumbbell[0001]}^{inter}$ (eV)	/2.87	2.85				

^a[1], ^b[2], ^c[3], ^d[4], ^e[5], ^f[6], ^g[7]

III. AL

RANN predicts the material properties for pure Al to be near that of DFT calculations as seen in [Table IV](#). RANN predictions for the generalized stacking fault energy (GSFE) along the $[112]$ direction in the (111) plane can be seen in [Fig. 1](#).

Table IV. Pure Al properties: *italic* are from previous DFT. a - lattice constant, E_c - cohesive energy, B is the bulk modulus, C - elastic constants, ΔE - structural energy difference, γ_{usf} - unstable stacking fault energy, γ_{ssf} stable stacking fault energy, $E_{surface}$ - surface energy, E^{vac} - vacancy formation energy, E^{inter} - interstitial energy.

Properties	Expt.	DFT	RANN
a (\AA)	4.05 ^a	4.04	4.04
E_c (eV)	3.39 ^b		3.36
B (GPa)	72.2 ^b	77.11	75.01
C_{11} (GPa)	114.3 ^b	<i>119.2^c, 114.6^c, 122.2^d, 110.4^e, 109.3^f, 101.0^g</i> , 110.93	94.63
C_{12} (GPa)	61.9 ^b	<i>64.3^c, 63.2^c, 60.8^d, 54.5^e, 57.5^f, 61.0^g</i> , 58.2	65.20
C_{44} (GPa)	31.6 ^b	<i>36.5^c, 35.3^c, 37.4^d, 31.3^e, 30.1^f, 25.4^g</i> , 32.2	46.14
$\Delta E_{fcc \rightarrow bcc}$ ($\frac{eV}{atom}$)		0.09	0.10
$\Delta E_{fcc \rightarrow hcp}$ ($\frac{eV}{atom}$)		0.03	0.03
$\Delta E_{fcc \rightarrow sc}$ ($\frac{eV}{atom}$)		0.37	0.37
$\Delta E_{fcc \rightarrow a15}$ ($\frac{eV}{atom}$)		0.08	0.08
$\Delta E_{fcc \rightarrow dc}$ ($\frac{eV}{atom}$)		0.74	0.75
$\Delta E_{fcc \rightarrow \omega}$ ($\frac{eV}{atom}$)		0.11	0.11
$\gamma_{usf}^{(110)[112]}$ ($\frac{mJ}{m^2}$)		<i>224^{h,i}</i> , 158.2	171.34
$\gamma_{ssf}^{(110)[112]}$ ($\frac{mJ}{m^2}$)	135-166 ^{b,j}	<i>122-164^{h,i,k}</i> , 125.9	123.88
$E_{surf}^{(001)}$ (eV)		873.8	926.69
$E_{surf}^{(110)}$ (eV)		927.7	968.80
$E_{surf}^{(111)}$ (eV)		820.2	846.27
E_f^{vac} (eV)	0.67 ^l	0.65	0.62
E_{tetra}^{inter} (eV)		3.21	3.21
E_{octa}^{inter} (eV)		2.84	2.92

^a[8], ^b[4], ^c[9], ^d[10], ^e[11], ^f[12], ^g[13], ^h[14], ⁱ[15], ^j[16], ^k[17–20], ^l[21]

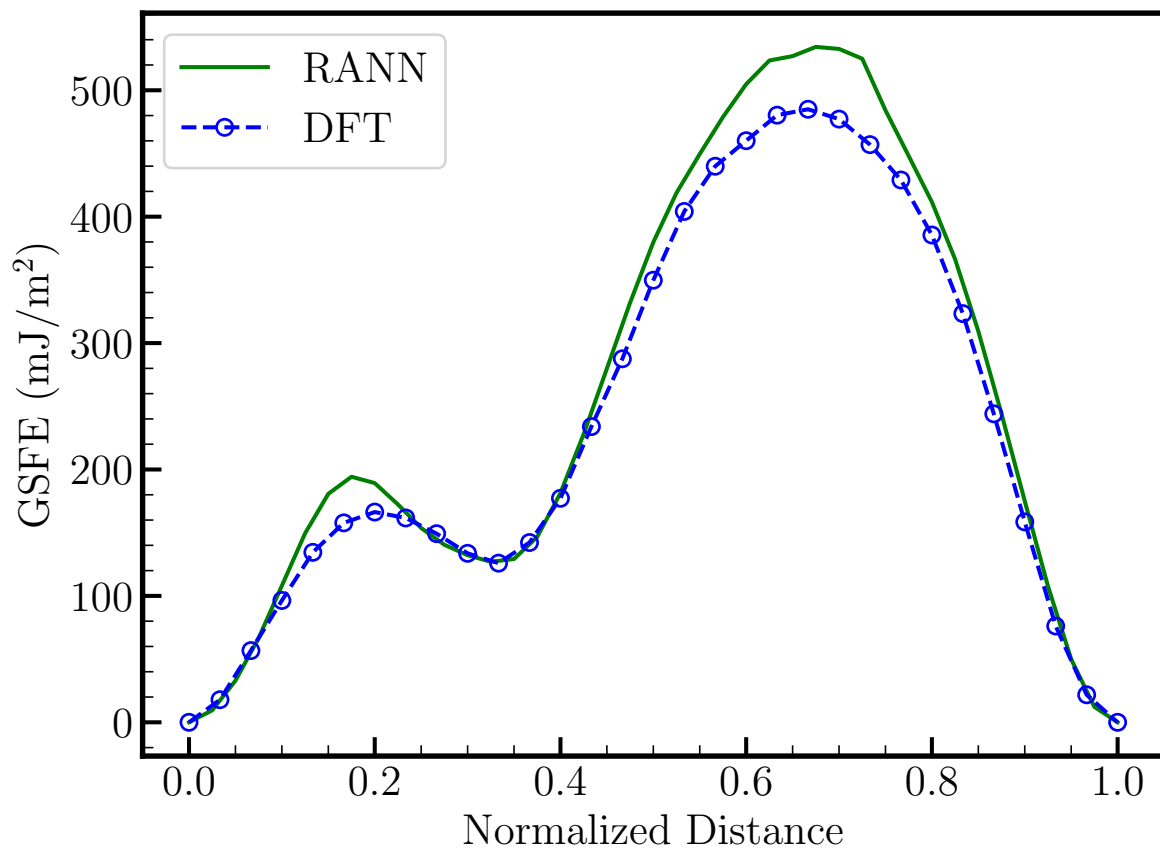


Figure 1. GSFE for pure Al along the $[112]$ direction in the (111) plane

IV. TI-AL

While MEAM [22] captures basic solid solution properties well, it fails to accurately predict plastic properties, such as the GSFE, for solid solutions. MTP [23] does well with GSFEs for formed intermetallics, but it also struggles with finding correct GSFEs for solid solutions. When adding an Al atom adjacent to the glide plane in the α phase, the GSFE is expected to decrease compared to that of pure α -Ti. The GSFE of pure α -Ti and Ti with one Al atom adjacent to the glide plane were calculated for both MEAM [22] and MTP. [23]. Structures ranging from 20-80 atoms with a fault plane approximately in the middle of the cell were created with the atomman Python package [24, 25]. Atoms above the fault plane were incrementally shifted in the x direction until the structure was back in the original configuration. Each structure was placed in a LAMMPS simulation with periodic boundary conditions in the x and y directions and a free surface in the z direction. The simulation fixed atoms in the x and y directions but allowed relaxation in the direction normal to the glide plane (z direction). Once the GSFE for pure α -Ti was calculated, one Ti atom was swapped to be an Al atom. Fig. 2 shows GSFE results for MEAM [22] and MTP [23] compared to DFT. MEAM shows this decrease in the GSFE, but underestimates the GSFE in the basal and prismatic planes. MTP predicts a higher GSFE when an Al atom is introduced adjacent to the glide plane. RANN shows both more accurate GSFEs and a decrease in the GSFE with the addition of an Al atom. This can be seen in Fig. 5 of the main article.

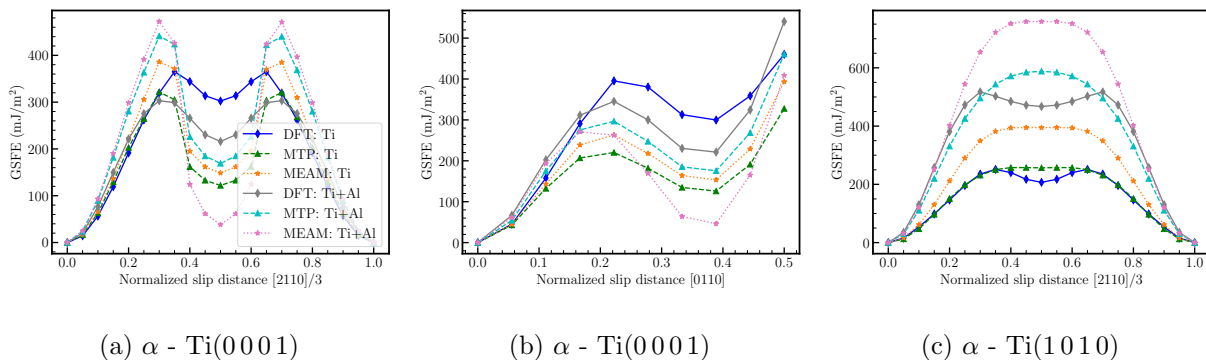


Figure 2. GSFE of Ti-Al alloy for DFT and MTP, where solute Al's position is in the first nearest positions relative to the glide plane)

The convex hull for RANN seen in Fig. 3 of the main text was found by allowing Ti-Al

structures of varying space groups to relax in a LAMMPS simulation. [Table V](#) displays energies from DFT and RANN for all structures and space groups tested. [Table VI](#) shows that

Table V. Formation energies of selected ordered structures (units of meV/atom) from both DFT and RANN potential.

Structure	Space group	DFT	RANN	Structure	Space group	DFT	RANN
Ti ₅ Al	$P6_32\bar{2}$	-137	-126	TiAl($B2$)	$Pm\bar{3}m$	-262	-290
Ti ₄ Al	$I4/m$	-179	-165	TiAl ($B8_1$)	$P6_3/mmc$	-252	-261
Ti ₃ Al($D0_{19}$)	$P6_3/mmc$	-281	-283	TiAl(B_h)	$P\bar{6}m2$	-251	-244
Ti ₃ Al($D0_{24}$)	$P6_3/mmc$	-268	-272	TiAl	$Fm\bar{3}m$	-173	-207
Ti ₃ Al($L1_2$)	$Pm\bar{3}m$	-264	-262	TiAl($B20$)	$P2_13$	-120	-134
Ti ₃ Al($D0_{22}$)	$I4/mmm$	-254	-243	TiAl ($B32$)	$Fd\bar{3}m$	-72	-95
Ti ₃ Al($D0_{23}$)	$I4/mmm$	-259	-251	Ti ₂ Al ₃	$P4/m$	-419	-418
Ti ₃ Al ($L2_1$)	$Fm\bar{3}m$	-144	-150	Ti ₂ Al ₃	$I4/mmm$	-310	-322
Ti ₅ Al ₂	$P4/mbm$	-54	-74	Ti ₂ Al ₃	$P4/mbm$	-73	-152
Ti ₁₁ Al ₅	$P4/mmm$	-236	-292	Ti ₃ Al ₅	$P4/mmm$	-283	-300
Ti ₂ Al ($B8_2$)	$P6_3/mmc$	-306	-304	Ti ₃ Al ₅	$P4/mmm$	-158	-195
Ti ₂ Al	$C2/m$	-268	-298	TiAl ₂ ($C14$)	$P6_3/mmc$	-318	-324
Ti ₂ Al ($C22$)	$P321$	-228	-224	TiAl ₂	$C2/m$	-244	-265
Ti ₂ Al($C40$)	$P6_222$	-269	-259	TiAl ₂	$I4/mmm$	-240	-252
Ti ₂ Al	$I4/mmm$	-143	-151	TiAl ₂ ($C38$)	$I4/mmm$	-231	-232
Ti ₂ Al ($C38$)	$I4/mmm$	-139	-180	TiAl ₂	$P4/mmm$	-41	-107
Ti ₂ Al	$Cmce$	-49	-59	TiAl ₂	$I4_1/amd$	-430	-430
Ti ₅ Al ₃	$P\bar{6}2m$	-116	-108	Ti ₂ Al ₅	$P4/mbm$	-290	-308
Ti ₃ Al ₂	$P4/m$	-332	-341	TiAl ₃ ($D0_{22}$)	$I4/mmm$	-398	-394
Ti ₃ Al ₂ ($D5_a$)	$P4/mbm$	-245	-241	TiAl ₃ ($D0_{24}$)	$P6_3/mmc$	-339	-374
Ti ₄ Al ₃	$P6_3/m$	-329	-313	TiAl ₃ ($D0_{19}$)	$P6_3/mmc$	-320	-327
Ti ₄ Al ₃	$I4/mmm$	-217	-223	TiAl ₃ ($D0_{23}$)	$I4/mmm$	-403	-410
TiAl($L1_0$)	$P4/mmm$	-405	-405	TiAl ₄ ($D1_a$)	$I4/m$	-217	-271
TiAl	$I4_1/amd$	-368	-369	TiAl ₅	$P6_32\bar{2}$	-182	-213

RANN is capable of modeling accurate material properties for the formed $D0_{19}$ structure.

[Table VII](#) shows that RANN is capable of reproducing near DFT results for the $L1_0$ material properties.

The α to $D0_{19}$ transition was examined with the MTP [23] potential using the semi-grand-canonical Monte Carlo (MC) method [35] as done in the work of Kim et al. [22]. This method adds a chemical potential difference term, $\Delta\mu$, to the Metropolis acceptance criterion [36] in order to determine if it is acceptable to swap one type of atom with another. Pure

Table VI. D0₁₉ properties : *italic* are from previous DFT.

Properties	Expt./DFT	RANN
a_0 (Å)	5.81 ^f / <i>5.76^e</i> ,5.74	5.74
c_0 (Å)	4.65 ^f / <i>4.66^e</i> ,4.64	4.64
c/a ratio	0.801 ^f / <i>0.81^e</i> ,0.81	0.81
C_{11} (GPa)	183 ^a / <i>221^b</i> , <i>185.8^c</i> , <i>184.7^d</i> , <i>192.2^e</i> ,197.42	204.6
C_{12} (GPa)	89 ^a / <i>71^b</i> , <i>76.6^c</i> , <i>82.4^d</i> , <i>80.5^e</i> ,78.56	74.74
C_{13} (GPa)	63 ^a / <i>85^b</i> , <i>60.1^c</i> , <i>63.4^d</i> , <i>62.5^e</i> ,66.24	71.95
C_{33} (GPa)	225 ^a / <i>238^b</i> , <i>225.2^c</i> , <i>225.1^d</i> , <i>232.9^e</i> ,234.86	234.07
C_{44} (GPa)	64 ^a / <i>69^b</i> , <i>57.2^c</i> , <i>54.0^d</i> , <i>61.6^e</i> ,66.63	72.99
C_{66} (GPa)	47 ^a / <i>75^b</i> , <i>54.6^c</i> , <i>51.2^d</i> , <i>55.85^e</i> ,59.43	64.94
$C_{12} - C_{66}$ (GPa)	42 ^a / <i>-4^b</i> , <i>22.0^c</i> , <i>31.2^d</i> , <i>24.65^e</i> ,19.03	9.8
$C_{13} - C_{44}$ (GPa)	-1 ^a / <i>16^b</i> , <i>2.9^c</i> , <i>9.4^d</i> , <i>0.9^e</i> ,-0.39	-1.04
$E_{\text{surf}}^{\{0001\}}$ ($\frac{mJ}{m^2}$)	/1.952	1.968
$E_{\text{surf}}^{\{1\bar{1}00\}}$ ($\frac{mJ}{m^2}$)	/2.313	2.254
$E_{\text{surf}}^{\{11\bar{2}1\}}$ ($\frac{mJ}{m^2}$)	/2.121	2.113
T_{melt} (K)		2256.27

^a[26], ^b[27], ^c[28], ^d[29], ^e[30], ^f[31]

Table VII. L1₀ properties : *italic* are from previous DFT.

Properties	Expt./DFT	RANN
a_0 (Å)	3.997 ^a / <i>3.996^f</i> ,3.98	3.98
c_0 (Å)	4.077 ^a / <i>4.076^f</i> ,4.07	4.07
c/a ratio	1.02 ^a / <i>1.02^f</i> ,1.02	1.02
C_{11} (GPa)	187 ^b / <i>190^c</i> , <i>170^d</i> , <i>164^e</i> , <i>167.4^f</i> ,168.92	170.62
C_{12} (GPa)	74.8 ^b / <i>105^c</i> , <i>88^d</i> , <i>85.5^e</i> , <i>87.7^f</i> ,87.2	92.93
C_{13} (GPa)	74.8 ^b / <i>90^c</i> , <i>84^d</i> , <i>81^e</i> , <i>86.1^f</i> ,86.93	87.37
C_{33} (GPa)	182 ^b / <i>185^c</i> , <i>179^d</i> , <i>178.6^e</i> , <i>169.14^f</i>	176.21
C_{44} (GPa)	109 ^b / <i>120^c</i> , <i>115^d</i> , <i>109.6^e</i> , <i>111.1^f</i> ,110.33	102.54
C_{66} (GPa)	81.2 ^b / <i>50^c</i> , <i>72^d</i> , <i>72.6^e</i> , <i>73.7^f</i> ,70.15	65.09
$C_{12} - C_{66}$ (GPa)	-6.4 ^b / <i>55^c</i> , <i>16^d</i> , <i>12.19^e</i> , <i>14^f</i> ,22.78	27.84
$C_{13} - C_{44}$ (GPa)	-34.2 ^b / <i>-30^c</i> , <i>-31^d</i> , <i>-28.6^e</i> , <i>-25^f</i> ,-22.96	-15.18
$E_{\text{surf}}^{\{100\}}$ ($\frac{mJ}{m^2}$)	/1.643	1.798
$E_{\text{surf}}^{\{111\}}$ ($\frac{mJ}{m^2}$)	/1.667	1.714
T_{melt} (K)		2279.11

^a[32], ^b[33], ^c[27], ^d[28], ^e[34], ^f[30]

α -Ti structures and D0₁₉ structures consisting of 1024 atoms were put under the semi-grand-canonical MC fix in LAMMPS at varying temperatures and $\Delta\mu$ values. A hysteresis loop is found by plotting the equilibrated atomic percentage of Al against the $\Delta\mu$ values. The transition point for a given temperature is taken to be the atomic percentage of Al that corresponds to the final data point before the original phase transforms. The MTP potential displays an accurate transition from the D0₁₉ phase to the α phase; however, it finds an intermediate phase going from the α phase to the D0₁₉ phase. This is evident in the hysteresis loop shown in Fig. 3 as the D0₁₉ phase jumps from roughly 25% Al to the α phase at roughly 3% Al, but the α phase does not directly jump to 25% Al. The α phase finds a stable structure around 15% Al before slowly reaching the D0₁₉ phase.

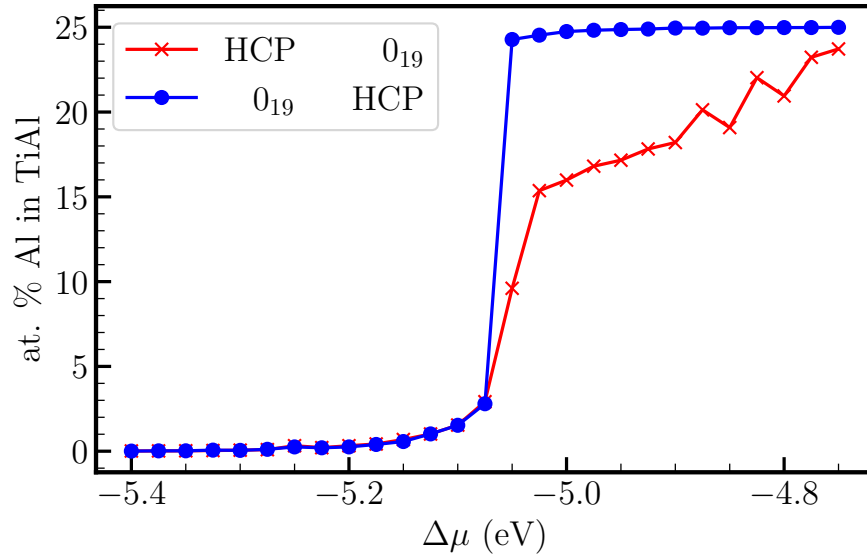


Figure 3. Semi-Grand-Canonical Monte Carlo Simulations for MTP [23] at 900 K.

REFERENCES

- [1] G. Simmons and H. Wang, “Single crystal elastic constants and calculated aggregate properties: a handbook,” (*No Title*), 1971.
- [2] B. Yin, Z. Wu, and W. Curtin, “Comprehensive first-principles study of stable stacking faults in hcp metals,” *Acta Materialia*, vol. 123, pp. 223–234, 2017.
- [3] M. S. Nitol, D. E. Dickel, and C. D. Barrett, “Machine learning models for predictive materials science from fundamental physics: An application to titanium and zirconium,” *Acta Materialia*, vol. 224, p. 117347, 2022.
- [4] C. Kittel, *Introduction to solid state physics*. John Wiley & sons, inc, 2005.
- [5] E. Fisher and C. Renken, “Single-crystal elastic moduli and the hcp \rightarrow bcc transformation in ti, zr, and hf,” *Physical review*, vol. 135, no. 2A, p. A482, 1964.
- [6] F. R. Boer, *Cohesion in metals: transition metal alloys*. North Holland, 1988, vol. 1.
- [7] W. Tyson and W. Miller, “Surface free energies of solid metals: Estimation from liquid surface tension measurements,” *Surface Science*, vol. 62, no. 1, pp. 267–276, 1977.
- [8] J. S. Blakemore, *Solid state physics*. Cambridge university press, 1985.
- [9] C. Malica and A. Dal Corso, “Quasi-harmonic temperature dependent elastic constants: applications to silicon, aluminum, and silver,” *Journal of Physics: Condensed Matter*, vol. 32, no. 31, p. 315902, 2020.
- [10] W. Li and T. Wang, “Ab initio investigation of the elasticity and stability of aluminium,” *Journal of Physics: Condensed Matter*, vol. 10, no. 43, p. 9889, 1998.
- [11] H. Wang and M. Li, “Ab initio calculations of second-, third-, and fourth-order elastic constants for single crystals,” *Physical review B*, vol. 79, no. 22, p. 224102, 2009.
- [12] R. Golesorkhtabar, P. Pavone, J. Spitaler, P. Puschnig, and C. Draxl, “Elastic: A tool for calculating second-order elastic constants from first principles,” *Computer Physics Communications*, vol. 184, no. 8, pp. 1861–1873, 2013.
- [13] S. Shang, A. Saengdeejing, Z. Mei, D. Kim, H. Zhang, S. Ganeshan, Y. Wang, and Z. Liu, “First-principles calculations of pure elements: Equations of state and elastic stiffness constants,” *Computational Materials Science*, vol. 48, no. 4, pp. 813–826, 2010.
- [14] G. Lu, N. Kioussis, V. V. Bulatov, and E. Kaxiras, “Generalized-stacking-fault energy surface and dislocation properties of aluminum,” *Physical Review B*, vol. 62, no. 5, p. 3099, 2000.

- [15] X.-Z. Wu, R. Wang, S.-F. Wang, and Q.-Y. Wei, “Ab initio calculations of generalized-stacking-fault energy surfaces and surface energies for fcc metals,” *Applied Surface Science*, vol. 256, no. 21, pp. 6345–6349, 2010.
- [16] R. Smallman and P. Dobson, “Stacking fault energy measurement from diffusion,” *Metallurgical Transactions*, vol. 1, pp. 2383–2389, 1970.
- [17] C. Woodward, D. Trinkle, L. Hector Jr, and D. Olmsted, “Prediction of dislocation cores in aluminum from density functional theory,” *Physical review letters*, vol. 100, no. 4, p. 045507, 2008.
- [18] S. Crampin, K. Hampel, D. Vvedensky, and J. MacLaren, “The calculation of stacking fault energies in close-packed metals,” *Journal of Materials Research*, vol. 5, pp. 2107–2119, 1990.
- [19] P. Denteneer and J. Soler, “Defect energetics in aluminium,” *Journal of Physics: Condensed Matter*, vol. 3, no. 45, p. 8777, 1991.
- [20] B. Hammer, K. Jacobsen, V. Milman, and M. Payne, “Stacking fault energies in aluminium,” *Journal of Physics: Condensed Matter*, vol. 4, no. 50, p. 10453, 1992.
- [21] T. Hehenkamp, “Absolute vacancy concentrations in noble metals and some of their alloys,” *Journal of Physics and Chemistry of Solids*, vol. 55, no. 10, pp. 907–915, 1994.
- [22] Y.-K. Kim, H.-K. Kim, W.-S. Jung, and B.-J. Lee, “Atomistic modeling of the ti–al binary system,” *Computational materials science*, vol. 119, pp. 1–8, 2016.
- [23] J. Qi, Z. Aitken, Q. Pei, A. M. Z. Tan, Y. Zuo, M. Jhon, S. Quek, T. Wen, Z. Wu, and S. P. Ong, “Machine learning moment tensor potential for modelling dislocation and fracture in $\text{Al}_{10}\text{-Ti}_{11}$ and $\text{d}_{019}\text{-Ti}_{3}\text{Al}$ alloys,” *arXiv preprint arXiv:2305.11825*, 2023.
- [24] C. A. Becker, F. Tavazza, Z. T. Trautt, and R. A. Buarque de Macedo, “Considerations for choosing and using force fields and interatomic potentials in materials science and engineering,” *Current Opinion in Solid State and Materials Science*, vol. 17, no. 6, pp. 277–283, 2013, *frontiers in Methods for Materials Simulations*. [Online]. Available: <https://www.sciencedirect.com/science/article/pii/S1359028613000788>
- [25] L. M. Hale, Z. T. Trautt, and C. A. Becker, “Evaluating variability with atomistic simulations: the effect of potential and calculation methodology on the modeling of lattice and elastic constants,” *Modelling and Simulation in Materials Science and Engineering*, vol. 26, no. 5, p. 055003, may 2018. [Online]. Available: <https://dx.doi.org/10.1088/1361-651X/aabc05>
- [26] K. Tanaka, K. Okamoto, H. Inui, Y. Minonishi, M. Yamaguchi, and M. Koiwa, “Elastic con-

- stants and their temperature dependence for the intermetallic compound Ti_3Al ,” *Philosophical Magazine A*, vol. 73, no. 5, pp. 1475–1488, 1996.
- [27] C. Fu and M. Yoo, “Elastic constants, fault energies, and dislocation reactions in tial: A first-principles total-energy investigation,” *Philosophical Magazine Letters*, vol. 62, no. 3, pp. 159–165, 1990.
- [28] Y. Liu, L. Liu, S. Wang, and H. Ye, “First-principles study of shear deformation in tial and ti_3al ,” *Intermetallics*, vol. 15, no. 3, pp. 428–435, 2007.
- [29] Y. Wei, Y. Zhang, G.-H. Lu, and H. Xu, “Site preference and elastic properties of a 2-ti 3 al with oxygen impurity: A first-principles study,” *International Journal of Modern Physics B*, vol. 24, no. 15n16, pp. 2749–2755, 2010.
- [30] C. Zhang, H. Hou, Y. Zhao, X. Yang, and Y. Guo, “First-principles study on structural, elastic and thermal properties of γ -tial and α_2 - Ti_3Al phases in tial-based alloy under high pressure,” *International Journal of Modern Physics B*, vol. 31, no. 11, p. 1750079, 2017.
- [31] W. B. Pearson, *A handbook of lattice spacings and structures of metals and alloys: International series of monographs on metal physics and physical metallurgy, Vol. 4*. Elsevier, 2013, vol. 4.
- [32] Q.-X. Pei, M. Jhon, S. S. Quek, and Z. Wu, “A systematic study of interatomic potentials for mechanical behaviours of ti-al alloys,” *Computational Materials Science*, vol. 188, p. 110239, 2021.
- [33] K. Tanaka, “Single-crystal elastic constants of γ -tial,” *Philosophical magazine letters*, vol. 73, no. 2, pp. 71–78, 1996.
- [34] H. Fu, Z. Zhao, W. Liu, F. Peng, T. Gao, and X. Cheng, “Ab initio calculations of elastic constants and thermodynamic properties of γ tial under high pressures,” *Intermetallics*, vol. 18, no. 5, pp. 761–766, 2010.
- [35] B. Sadigh, P. Erhart, A. Stukowski, A. Caro, E. Martinez, and L. Zepeda-Ruiz, “Scalable parallel monte carlo algorithm for atomistic simulations of precipitation in alloys,” *Physical Review B*, vol. 85, no. 18, p. 184203, 2012.
- [36] N. Metropolis, A. W. Rosenbluth, M. N. Rosenbluth, A. H. Teller, and E. Teller, “Equation of state calculations by fast computing machines,” *The journal of chemical physics*, vol. 21, no. 6, pp. 1087–1092, 1953.